From THE DEPARTMENT OF CLINICAL NEUROSCIENCE
Karolinska Institutet, Stockholm, Sweden

METHODOLOGICAL DEVELOPMENTS IN SMALL ANIMAL PET NEUROIMAGING

Miklós Tóth

Karolinska Institutet

Stockholm 2015

Cover Illustration:

Illustrating the underlying digital nature of MRI and PET imaging with a post processed rodent multimodal image.

Published by Karolinska Institutet.
Printed by Åtta.45 tryckeri AB

ISBN 978-91-7549-940-6

Methodological developments in small animal PET neuroimaging
THESIS FOR DOCTORAL DEGREE (Ph.D.)

By

Miklós Tóth

Principal Supervisor:
Professor Balázs Gulyás
Karolinska Institutet
Department of Clinical Neuroscience
Centre for Psychiatry Research

Co-supervisors:
Professor Christer Halldin
Karolinska Institutet
Department of Clinical Neuroscience
Centre for Psychiatry Research

Associate Professor Andrea Varrone
Karolinska Institutet
Department of Clinical Neuroscience
Centre for Psychiatry Research

Opponent:
Professor Anne Roivainen
University of Turku
Turku PET Centre
Turku, Finnland

Examination Board:
Professor Brun Ulfhake
Karolinska Institutet
Department of Neuroscience

Docent Claudia Kuntner
Austrian Institute of Technology
Department of Health & Environment
Vienna, Austria

Senior Lecturer Greg Mullen
King's College London
Faculty of Life Sciences & Medicine
London, United Kingdom

To my family

ABSTRACT

Positron emission tomography (PET) is a nuclear imaging technique using a multidisciplinary approach to functionally visualize processes in the brain or other living tissue. It is capable to determine the pharmacokinetic and pharmacodynamic properties of a molecule in the CNS, with a low risk of side effects on the subject. This is executed through injection of a radioactively labeled substance into the subject and detection of released gamma photons after radioactive decay of the molecule in the target organ or tissue. Based on these detections, it is possible to reconstruct the distribution of radioligand in the living tissue into an image representing the physiology of the subject.

The present thesis focuses on the methodological development of PET imaging in small animal research and on the support for connecting basic research to human health-related clinical applications in neuroscience. The work underlying this thesis work is divided into three sections. Section 1 consists of the validation of a new PET/MRI small animal imaging system. Since the combination of an MRI magnet with a conventional PET ring could influence the performance of PET measurements, a combined system should be implemented with special care. The results of Study I showed that the combination of PET and MRI components did not affect the performance of the final system and it is capable to effectively conduct consecutive multimodal imaging with functional images from PET and anatomical information of soft tissue. After the validation of the PET system used in this thesis work for imaging, in Section 2 different methodological challenges are presented. Study II focuses on the transporter activity of the blood-brain barrier to highlight the necessity of proper animal model selection while designing pre-clinical PET studies, while in Study III we offer a solution for longitudinal [^{11}C]PBR28 imaging with the validation of SUV as an outcome measure in rodents studies, where blood sampling is a difficult task. Within Section 3 a new animal model and a novel ligand is presented. The previously validated SUV approach from Study III is applied in Study IV during the longitudinal follow-up of the M2CAO stroke rat model to measure changes in the TSPO signal as a mark of neuroinflammation after cortical ischemia. In Study V a knockout animal model was used to validate the novel radioligand [^{11}C]T-773, which was confirmed to bind selectively to the PDE10A enzyme and its distribution and uptake proves its suitability in small animal research.

In conclusion the thesis focuses on the development of novel methodological platforms for small animal imaging PET with the aim to provide advancements in the field of translational neuroscience.

LIST OF THESIS PUBLICATIONS

I. Nagy K, **Tóth M**, Major P, Patay G, Egri G, Häggkvist J, Varrone A, Farde L, Halldin C, Gulyás B.
Performance evaluation of the small-animal nanoScan PET/MRI system.
J Nucl Med. 2013; 54(10): 1825-32

II. **Tóth M**, Häggkvist J, Varrone A, Finnema SJ, Doorduin J, Tokunaga M, Higuchi M, Gulyás B, Halldin C.
ABC transporter-dependent brain uptake of the 5-HT_{1B} receptor radioligand [^{11}C]AZ10419369: a comparative PET study in mouse, rat, and guinea pig.
EJNMMI Research. 2014; 4:64

III. **Tóth M**, Doorduin J, Häggkvist J, Varrone A, Amini N, Halldin C, Gulyás B.
Positron Emission Tomography studies with [^{11}C]PBR28 in the healthy rodent brain: validating SUV as an outcome measure of neuroinflammation.
PLOS ONE, in press (manuscript format)

IV. **Tóth M**, Little P, Arnberg F, Häggkvist J, Mulder J, Halldin C, Gulyás B, Holmin S.
Acute neuroinflammation in a clinically relevant focal cortical ischemic stroke model in rat: Longitudinal positron emission tomography and immunofluorescent tracking.
Brain Struct Funct. 2015 (epub ahead of print)

V. **Tóth M**, Häggkvist J Stepanov V, Takano A, Nakao R, Amini Nahid, Miura S, Kimura H, Taniguchi T, Gulyás B, Halldin C.
Molecular Imaging of PDE10A Knockout Mice with a Novel PET Radiotracer: [^{11}C]T-773.
Mol Imaging Biol. 2015 (epub ahead of print)

CONTENTS

LIST OF ABBREVIATIONS

2-TCM	Two-tissue compartment model
3D	Three-dimensional (x, y, z spatial dimensions)
3-TCM	Three-tissue compartment model
4D	Four-dimensional (x, y, z spatial dimensions and time as fourth dimension)
5-HT_{1B}	5-hydroxytryptamine receptor 1B
ABC transporter	ATP binding cassette transporter
ATP	Adenosine triphosphate
BBB	Blood-brain barrier
BCRP	Breast cancer resistance protein
BP	Binding potential
C_{FT}	Free concentration in tissue
C_{ND}	Non-displacable bound concentration
C_{NS}	Non-specifically bound concentration
C_P	Concentration in plasma
C_S	Specifically bound concentration
CsA	Cyclosporin A
CT	X-ray computed tomography
e^+	Positron
FOV	Field of view
GFAP	Glial fibrillary acidic protein
HD	Huntington's disease
HET	Heterozygous
HMGB1	High-mobility group box 1 protein
HOM	Homozygous
HPLC	High performance liquid chromatography
i.v.	Intravenous
IF	Immunofluorescence
IL-1β	Interleukin-1 β
LYSO:Ce	Lutetium yttrium orthosilicate:cerium

M2CAO	Occlusion of the M2-segment of the middle cerebral artery
MLEM	Maximum likelihood-expectation maximization
MRI	Magnetic resonance imaging
Mrp	Multidrug resistance-associated protein
NMR	Nuclear magnetic resonance signal
PET	Positron Emission Tomography
P-gp	P-glycoprotein
ROI	Region of interest
SRTM	Simplified reference tissue model
StAR	Steroidogenic acute regulatory protein
TAC	Time activity curves
TNFα	Tumor necrosis factor α
VOI	Volume of interest
V_T	Total distribution volume
WILD	Wild type

1 INTRODUCTION

It is often challenging to find a direct connection between basic biomedical research and human health. It is therefore of crucial importance that we find appropriate ways to translate results, obtained in basic biomedical research, to human health care, including clinical diagnostic and therapeutic applications. With the help of translational research we are able to facilitate this connection through the refinement of our research tools, methods and animal models to advance results in applied sciences. The focus of the present thesis was to improve the available tools for translational research in neurological and psychiatric diseases.

To conduct the presented experiments in this thesis work one should have relevant knowledge in the field of physics, chemistry, pharmacy, biology and medicine consequently it is important to emphasize that the present thesis work could have not been realized without the joint effort of an excellent multidisciplinary team.

1.1 FUNCTIONAL IMAGING - PRINCIPLES OF PET

Since the revolutionary discovery of Georg de Hevesy in the 1930s of using radioisotopes to monitor biological processes in the living organism, several methodologies have been developed to monitor the biochemical and physiological processes in the human body, including positron emission tomography (PET). PET is a nuclear imaging technique using a multidisciplinary approach to functionally visualize processes in the living tissue (*in vivo*). Due to its minimally invasive nature PET can determine the pharmacokinetic and pharmacodynamic properties of a drug candidate in the CNS with a low risk of side effects on the subject. In order to achieve this, the radiotracer is aimed to be administered in a microdosing manner *(1, 2)*.

1.1.1 Radiochemistry

A PET examination requires a substance labelled with a positron emitting radionuclide to be present at the exact site of investigation. PET radioligands are synthesized in order to fulfil this goal. It consists of a pharmacophore responsible for target interaction and a positron emitting radionuclide which helps during the detection of said interaction. Without suitable imaging probes we wouldn’t be able to detect the patterns of target distribution, metabolism and pharmacokinetic mechanisms within the living tissue.

To rationalize PET radioligand design and ideal candidate selection for CNS studies, several attributes of the pharmacophore have been selected as advantageous in order to achieve proper brain uptake, specific signal, and low background signal due to nonspecific binding or radiometabolites. Properties like mediocre lipophilicity, low molecular weight, high affinity and selectivity for the target with good clearance is generally preferred for brain studies in order for the pharmacophore to enter the blood-brain barrier (BBB) *(3)*. Recent progress in protein chemistry suggests the possibility of proteins as future imaging probes as well *(4)*.

1.1.1.1 Radionuclides

Production of radiotracers is done through a particle accelerator (cyclotron) bombarding atoms to produce a wide variety of radionuclides used during the labelling process. The most commonly used radionuclides are unstable isotopes of atoms found in the human body ^{15}O, ^{11}C, ^{13}N or ^{18}F. In the present thesis we have used the ^{11}C radionuclide for our PET investigations, it has a short half-life (20.39 min) with 99.8% β^+ decay *(3, 5)*.

1.1.1.2 Synthesis of radioligands

After preparation, the radionuclide is rapidly reacted with a precursor used in large excess. Through purification the final product is separated from any remaining non-labelled precursor by HPLC to achieve high specific radioactivity and to avoid residual toxic effects. The PET radioligand production process is finally monitored by quality control to ensure proper purity, sterility and pH. The final labelled molecule is named differently depending on its target or use: radioligand (when it is binding to a specific target), radiotracer (when there is no specific target, but processes like metabolism is examined) or radiopharmacon (when a drug is labelled).

1.1.2 PET data acquisition

The most common route to introduce a radioactive tracer *in vivo* is through an intravenous (i.v.) injection. The radioligand accumulates with time in the target tissue and through decay it emits a positron (e^+) which travels only a short distance (few millimetres, depending on the type of radionuclide) before losing its energy to the surrounding electron rich tissue. Through annihilation, the mass of an electron and the positron is converted into electromagnetic energy, which is released as two high-energy photons (511 keV) in a random direction 180º±0.25 º (non-collinearity) apart *(6)*. These high energy photons have a high chance to leave the body and therefore can be detected during PET measurements (Fig. 1).

The facts that photons travel in a line, creating a so called line of response, and that each photons detection time can be individually recorded, make it possible to separate random detection events from the hundreds of thousands coincidence events per second. It is the reconstruction algorithm's task to translate this enormous dataset of coincidence records into meaningful three-dimensional images (x, y, z spatial dimensions, 3D).

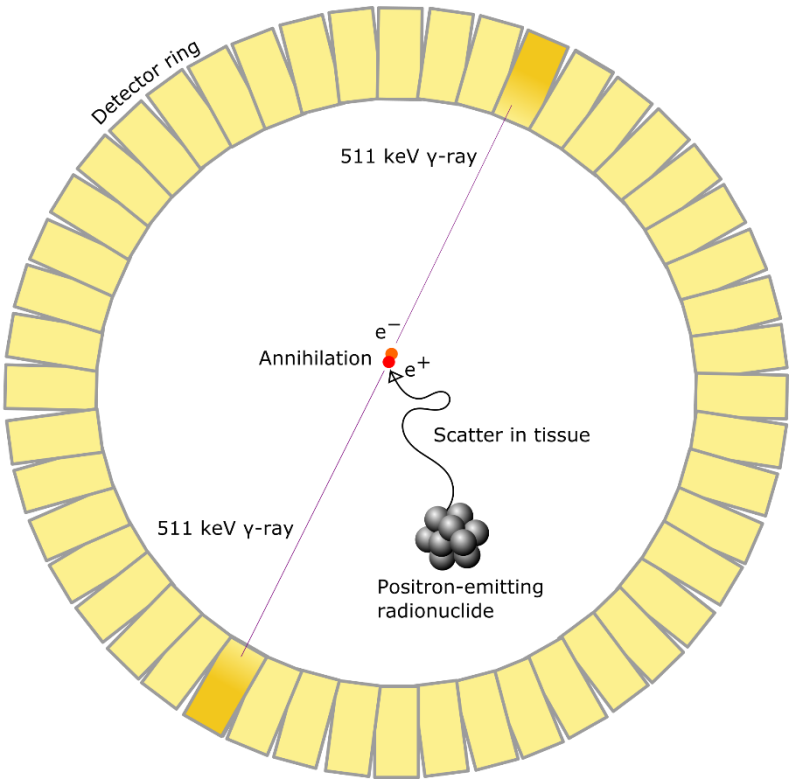

Figure 1. Schematic summary of radionuclide decay, positron scatter and photon detection in a PET ring.

1.1.3 PET data reconstruction

In order to calculate three dimensional images from the detected annihilations, many computational methods have been developed. Analytic methods like filtered back-projection and Fourier reconstruction has been extensively used for quantitative PET image reconstruction. These methods are based on the inherent assumption that the data is devoid of statistical noise, therefore currently used iterative methods which are counting for uncertainties of PET data (positron decay process, random events, hardware related etc.) by including data statistics in their modelling are proven to be more advantageous, albeit more computation heavy *(7)*.

In this thesis work we have used the maximum likelihood-expectation maximization (MLEM) algorithm *(8)*. Depending on the radioligand, typical PET measurements are ranging from 20 to 120 min. During this time interval the detection is continuous and the data set can be reconstructed into several timeframes (3D image segments) with different frame length to generate a dynamic PET image for analysis. After reconstruction the dynamic four-dimensional PET image (x, y, z spatial dimensions and time as fourth dimension, 4D) is representing the concentration of the radioligand in the field of view (FOV) as a function of time quantitatively.

1.1.4 Region of interest analysis

The reconstructed 4D PET images are used to generate regional time activity curves (TAC) by defining a region of interest (ROI) or volume of interest (VOI) over a specified area of the PET image. Each 3D image represents the average tracer concentration during the time

period, therefore averaging each voxel's uptake value within this VOI in every frame, presents the changes over time in the uptake of radioligand. Standard method of VOI delineation is done manually either directly on the PET image or on a reference anatomical image from the same animal. Depending on the amount and complexity of VOIs this may require an extensive amount of labour in case of each subject, with a high possible variability even with reference images available. Consequently, different template based methods have been developed requiring either linear or non-linear coregistration of PET to a reference space with premade VOI templates.

1.1.5 Quantification of radioligand receptor binding

To gain fully quantitative information on receptor binding, mathematical modelling of the regional TAC's kinetic properties is required. Several models have been created to describe the relationship between input to the tissue (radioligand concentration in plasma) and the induced response in said tissue (radioligand concentration in the target region) to define the behaviour of radioligands in the body. While the uptake of a ligand depends on its interaction with every organ, tissue, cell or molecule, each model incorporates assumptions and simplifications to reduce the parameters needed to be calculated.

After administration to the body, most radioligands leave the site of administration to enter a central compartment (like blood or plasma), from which it is exchanged with peripheral compartments (brain tissue) or eliminated through metabolism or excretion. This movement of radioligand from one compartment to another can be described by transfer rate constants and therefore in each compartment, characterized by its own volume, the radioligand concentrations are proportional to the amount of available tracer. For modelling purposes a compartment might include several organs or tissues if they behave uniformly. The multicompartmental model assumes homogenous radioligand concentration in the separate compartments where different parameters can be estimated through fitting the data (Fig. 2).

In order to fit the data several methods can be used, e.g. kinetic, equilibrium and graphical analysis, but within this thesis work only kinetic and graphical analyses were applied.

The two main outcome measures in quantification of receptor binding are total distribution volume (V_T) and binding potential (BP). V_T is the amount of plasma required to account for the amount of radioligand in 1 cm^3 of tissue, and therefore it is calculated as a ratio between the total tracer concentration in tissue and in plasma at equilibrium. Binding potential is defined as the ratio between receptor density (B_{max}) and the equilibrium dissociation constant (K_D). It aims to quantify the equilibrium concentration of specific binding in the target region as a ratio to some other reference concentration, like plasma (BP_P) or non-displaceable radioligand in tissue (BP_{ND}) *(9)*.

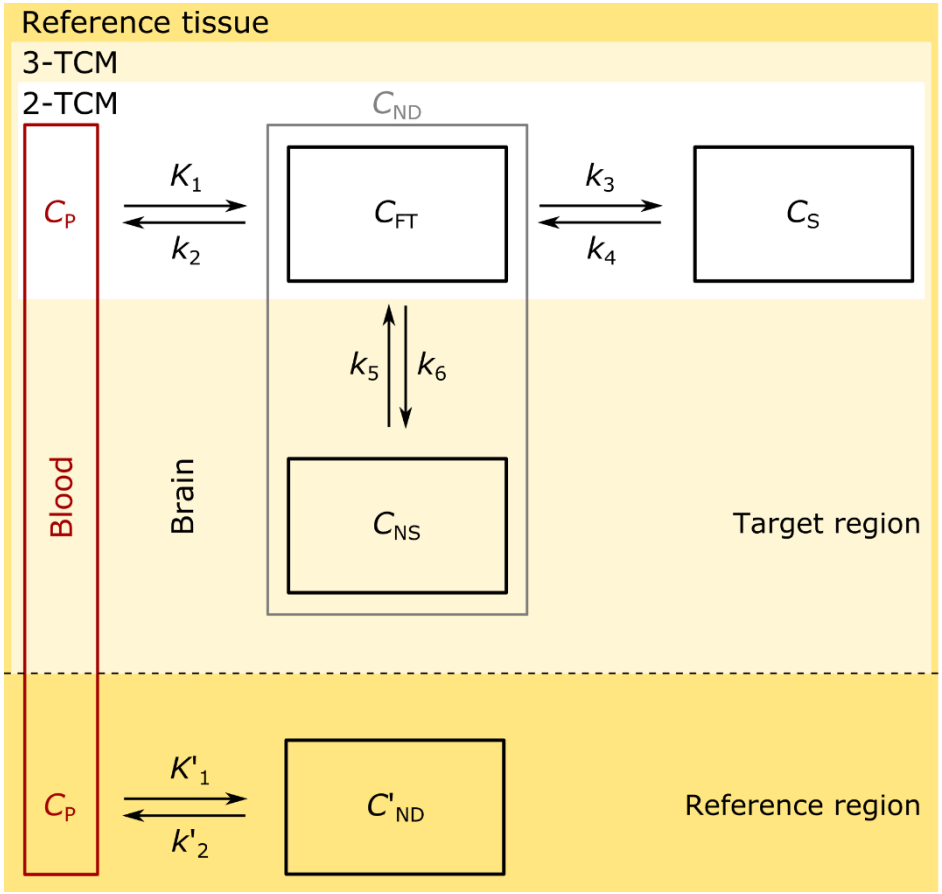

Figure 2. Schematic graph of compartmental models (2-TCM, 3-TCM and reference tissue modelling) used during kinetic analysis in brain PET studies. *C* represents the concentration of radioligand in the following compartments: C_S – specifically bound, C_{FT} – free in tissue, C_{NS} – non-specifically bound, C_{ND} – non-displaceable, C_P – plasma. K_1, k_2, k_3, k_4, k_5, k_6, K'_1 and k'_2 are kinetic rate constants between the different compartments.

1.1.5.1 Three- and Two-tissue compartment model

The data measured in a dynamic PET measurement is the sum of all compartments interaction. One of the most basic model, the three-tissue compartment model (3-TCM) aims to distinguish the different forms of tracer in tissue and ends up with a model that contains six unknown parameters, K_1 to k_6. The two-tissue compartment model (2-TCM) is a simplified version of the 3-TCM to reduce the large number of model parameters required to be estimated, which often would increase the variance of the resulting parameters and tends to be too high for reliable interpretation. In order to reduce the parameters in the 2-TCM, free and non-specifically bound tracer concentration is treated as a single compartment C_{ND} (non-displaceable concentration) under the assumption that the exchange between C_{FT} (free concentration in tissue) and C_{NS} (non-specifically bound concentration) is significantly faster than the exchange between C_{FT} and C_S (specifically bound concentration) (Fig. 2).

1.1.5.2 Logan graphical analysis

The Logan plot is a graphical analysis technique developed for reversible receptor systems to estimate V_T. The measured TAC in the target region is plotted against the measured and integrated plasma activity *(10)*. It fits a linear curve instead of using iterative curve fitting

methods, and therefore it is much less demanding computationally. The Logan plot will reach a straight line after sufficient equilibration time and the slope represents the total distribution volume V_T *(11)*. Due to the required blood sampling to estimate the input activity to the tissue through compartment C_P, the Logan plot is often referred to as invasive Logan plot.

1.1.5.3 Simplified reference tissue model

In order to estimate V_T with 2-TCM or Logan plot the radioactivity concentration in plasma is required to be measured. Due to the invasiveness of an arterial blood measurement, estimation of radioligand binding within the tissue can be helpful and preferred in cases where a reference region is available. The main requirement for a proper reference region is to be devoid of the target and therefore no specific binding is present and could be described by the C'_{ND} compartment only.

The simplified reference tissue model (SRTM) is a further development of the 4 parameter reference tissue model developed by Lammertsma et al. *(12)*. It reduces the number of fitted parameters from four to three by introducing two additional assumptions: $C_{ND} = C'_{ND}$, meaning that the distribution volume of non-displaceable bound radioligand is the same in the target region and in the reference region; and that the reference tissue can be fitted by a 1-tissue compartment model. Due to these modifications the model calculates only three parameters R_1, k_2 and $BP_{ND,}$ using nonlinear regression techniques with increased convergence rate and stability versus the 4 parameter reference tissue model. In this model R_1 is the ratio between K_1 and K'_1 while BP_{ND} is the outcome parameter *(13)*.

1.2 ANATOMICAL IMAGING

The contribution of PET imaging on revealing the function of a living tissue is outstanding. It is not only capable to differentiate between areas of high/low receptor density, changes in metabolism or tissue functions in the subject, but able to follow changes longitudinally as well. Depending on the target, the signal in a PET image might be originating from a specific tissue or could be more general, with only small differences between anatomical areas of the body. Even though the resolution of PET is constantly improving, its inherent limitation on good spatial resolution and the fact that distinct regions of the body could have similar functions with some of the radioligands, images from a PET measurement frequently lacks the information for an accurate regional identification and quantification. To circumvent the aforementioned issues, PET imaging is usually coupled with anatomical imaging. Both magnetic resonance imaging (MRI) and X-ray computed tomography (commonly referred to as CT) is commonly coupled with PET to acquire anatomical details. With these imaging techniques it is possible to achieve sub-millimetre resolutions and therefore to provide sufficient reference information.

1.2.1 CT

The first modality used to provide extra anatomical information for PET was CT imaging, due to its high spatial resolution and already well-established use in oncology research *(14)*.

During a CT measurement, an X-ray source is rotated around the subject while the X-ray sensor is placed opposite from the source to collect information from the body. When X-rays penetrate through tissue there is a certain likelihood that it will get absorbed based on electron density. CT produces a topographic data volume similar to PET which can be used to show different structures of the body differentiated based on their ability to block the projected X-ray. CT imaging is mostly used in bone and lung investigations, but several other diagnostic methods are used as well, where rapid imaging coupled with high resolution is required, like cardiac CT.

Besides the anatomical information, CT imaging has another important application attributed to similar absorption mechanisms between PET and CT. Although the X-rays have less energy than gamma-rays, images from CT measurements can be used as an absorption map for attenuation correction to account for quantification error originating from gamma photon absorption in PET *(15)*.

Despite the usefulness of CT imaging, one major drawback is that radiation load from CT imaging can be an issue in longitudinal studies as significant doses (0.6 Gy, 5% of LD 50) can be measured in mice even after one whole-body high resolution CT scan *(16)*.

1.2.2 MRI

Opposed to PET and CT imaging, MRI does not use the higher energy parts of the electromagnetic spectrum (gamma-rays, X-rays, etc.), but applies non-ionizing low energy radio waves coupled with a magnetic field to create images of the subject. In CT, the required radiation dose for good image quality is quite significant *(17)*, thus MRI has an advantage over CT in general due to decreased radiation load.

During MRI imaging, each proton in the subject positioned within a magnetic field is excited by a radio frequency pulse, while this energy is lost the tissue produces a nuclear magnetic resonance signal (NMR) which can be detected. Gradient coils around the subject make it possible to modulate the main magnetic field and therefore to make the NMR signal encode positional information also providing the precondition for 3D volume generation.

While the drawback of MRI imaging compared to CT is longer acquisition time, it is preferred over CT thanks to the increased soft tissue contrast. This parameter is exceptionally important in brain studies, where white and grey matter separation is the most common way for gaining anatomical orientation in the tissue. The different properties of MRI imaging provide numerous options to emphasize the different characteristics of the tissue in our interest. While the most common method is T_1 weighted imaging where cerebrospinal fluid (CSF) is black, but it is similarly easy to acquire a T_2 weighted image with high intensity signal from CSF and damaged tissue. Even though the good soft tissue contrast made MRI the ideal technique for investigating the anatomy of the central nervous system, it has a wide array of options for functional imaging like spectroscopy, blood-oxygen-level dependent functional MRI or diffusion weighted imaging.

One obstacle of MRI as a complementary imaging for PET, is that the MRI data doesn't easily translate into absorption maps. MR imaging contains information about proton density in the tissue and not electron density, therefore it is not easily applicable as an attenuation map. The biggest issue is bone and air separation considering neither bone tissue nor air has signal in MRI due to low proton density while bone tissue shows high absorption signal in CT. Though it is possible to set up an automatic segmentation map based on a-priori knowledge, this method is mostly applicable on body parts that are rigid and have relatively small variations *(18)*.

1.3 MULTIMODAL IMAGING IN CNS RESEARCH

Multimodal imaging systems in small animal research are combining PET with many different modalities like single-photon emission computed tomography (SPECT), CT or MRI. While PET/SPECT provides the possibility to conduct studies with multiple radioligands, its usefulness has been less apparent than the combination of PET/CT or PET/MRI.

Combination of PET/CT has significant advantage over a standalone PET due to high resolution anatomical information coupled with shorter scan times and fast attenuation correction measurements. CT based attenuation correction has higher statistics/lower noise compared to traditional attenuation measured with gamma sources, but CT based attenuation might produce movement related artefacts. These artefacts can lead to an erroneous PET measurement calibration. The issue of high radiation doses from CT measurements coupled with the low soft-tissue contrast for anatomical mapping, created the need for PET/MRI imaging systems in molecular imaging investigations.

Currently PET and CT scans are conducted consecutively and the integration of PET detectors inside the CT seems impossible due to the high X-ray flux. Although integration of a PET ring inside an MRI is fundamentally possible and during the past years serious efforts have been made to implement it *(19, 20)*, it still requires further refinements. Another path for an integrated PET/MRI system is similar to the design of PET/CT, the two systems built next to each other for consecutive imaging. Within this thesis work the integration and application of a small animal PET ring on a 1 Tesla magnet is presented.

1.4 DIFFERENCES BETWEEN CLINICAL AND PRE-CLINICAL IMAGING

Largest differences between clinical and pre-clinical imaging are originating from the size of the subject aimed to be investigated. For small rodents like a mouse or rat, decreased PET ring size is not just possible, but preferable, as a small bore size results in higher sensitivity and resolution. Higher sensitivity is achieved by the increased size of the angle covered by an individual detector element resulting in larger detection solid angle, while the resolution increase is the direct result of reduced non-collinearity effect. Although a smaller PET ring has the drawback of faster decline in spatial resolution away from the centre of FOV, it achieves much higher resolutions in the centre compared to clinical scanners. Resolution of small animal imaging systems are around 1-1.5 mm full width at half maximum (FWHM),

while the current clinical scanners are around 3-5 mm FWHM *(21, 22)*. The only clinical system that can achieve comparable resolution with pre-clinical imaging with 1.5 mm FWHM is the High Resolution Research Tomograph (HRRT) of CTI-Siemens, which is built with decreased bore size as well, primarily for brain imaging *(23)*. As the systems used in small animal imaging include smaller detector elements/detector ring it significantly reduces the error originating from photon non-collinearity, thus modelling of positron range becomes a significant importance in increasing the spatial resolution. This is usually implemented in the reconstruction algorithm for more accurate imaging.

Even though the achievable resolution is higher in small animal PET compared to clinical PET imaging solutions, we should not forget the large differences in size between humans and rodents. This creates a challenge for several aspects of PET imaging in small animals. This is especially true for brain imaging where the size of the human brain is several hundred times larger than in rodents. The average brain weight of a human is around 1200-1400g, while the average rat and mouse brain is around 2-3g and 0.3-0.5g respectively *(24)*. The lower relative resolution of small animal imaging due to size differences, results in spill over and partial volume effects as well as it presents a challenge in application of automatic coregistration methods for multimodal imaging. This results in labour intensive manual registration of PET images to brain atlases or individual MRI images.

The decreased body size has an additional drawback for PET quantification due to significantly smaller available blood pool during input curve estimation for invasive modelling methods.

1.5 TARGET SYSTEMS IN PET

One of the advantages of PET is the diversity of the different mechanisms/targets that can be observed by this imaging technique. Receptor-ligand interactions are the most commonly examined processes with PET, while blood flow measurements or different enzymatic reactions either intra- or extracellularly can be followed as well. This molecular imaging technique is capable of revealing metabolism, protein synthesis and tissue signalling or even the progression of some diseases over time.

Apart from imaging the direct interaction of specific molecules and target proteins with radioligands, radiotracers are aimed to be used in a more passive manner. Radiotracers like [^{15}O]water or [^{11}C]butanol can be used as a tool to estimate cerebral blood flow based on their passive distribution within the tissue *(25)*, while the glucose analogue [^{18}F]FDG is a widely used tracer to measure glucose metabolism, as its accumulation depends mostly on the glucose uptake and phosphorylation activity of the tissue. The most frequent application of [^{18}F]FDG is in tumour imaging, even though newer, more specific radiotracers or radioligands are continuously developed *(26)*.

Within this thesis work phosphodiesterase 10A (PDE10A) and translocator protein (TSPO) radioligands have been used together with a 5-hydroxytryptamine receptor 1B (5-HT$_{1B}$) ligand to investigate BBB interaction through transporter modulation.

1.5.1 The blood-brain barrier

Species differences may result in significant variations between the efficacies of the same drug in different species. Therefore the metabolic, pharmacokinetic and toxicological data obtained in small animals should be extrapolated to other species or to humans with care. Such differences could originate from various factors like metabolism, resulting from the genetic variations in drug-metabolizing enzymes, which in turn may alter pharmacokinetics, drug clearance, drug efficacy and safety *(27)*. Another possible factor resulting in species differences is related to the differences in the transport of drug molecules either in the periphery, in organs such as the liver, kidney and gastrointestinal tract or in the central nervous system across the BBB *(28–30)*.

As a general consensus the BBB is perceived as a barrier consisting of neuronal and vascular units protecting the brain tissue from toxic substances by their unique interaction *(31)*. In the brain capillaries the BBB is built up by the interaction of endothelial cells and astrocytes, where the integration of neuronal projections through pericytes make vasodilatation regulation possible as well *(32)* (Fig. 3). Within this specific tissue composition endothelial cells are separating the blood compartment from the brain tissue. Through tight junctions between endothelial cells and by additional mechanisms like specific transporter systems within the plasma membrane the endothelial cells are capable to regulate the entry of larger molecules. While small or lipophilic molecules might enter the brain by passive diffusion *(33)*, endothelial cells are limiting the paracellular flow of larger molecules by forming tight junctions between their membranes. The integrity and expression of tight junction proteins (occludin, claudin-5) is a crucial factor which has been shown to be regulated by gut microbiota *(34)*. Besides blocking paracellular flow, endothelial cells are regulating transcellular flow as well by intracellular elements like enzymes, and membrane transporters. In order to help investigations of drug delivery or intervention efficacy, different methods have been used for BBB disruption (osmotic, ultrasound, bradykinin administration, radiation) or BBB circumvention (viral mediated, carrier molecule, liposomal delivery, plasma membrane transporter modulation) *(35)*.

Transporters in the plasma membrane of endothelial cells are becoming the main interest for BBB transporter function modulation. Largest family of transporters are belonging to the adenosine triphosphate (ATP)-binding cassette (ABC) superfamily, which includes 49 genes divided into seven sub-families (designated ABCA–ABCG) encoding the various ABC transporters in the human genome *(36, 37)*. Three ABC subfamilies (B, C, and G) contain ATP mediated efflux pumps, which are involved in metabolite and xenobiotic transport throughout the barrier and excretory tissues in the body (blood and testis barrier, placenta, lung, gastrointestinal tract, liver, kidney), influencing the pharmacokinetics of many signal molecules, metabolites, toxins and therapeutic drugs *(38)*. In the brain tissue the presence of the following subfamilies has been shown: ABCB1, ABCC1, ABCC2, ABCC4, ABCC5, ABCG2 *(36)*.

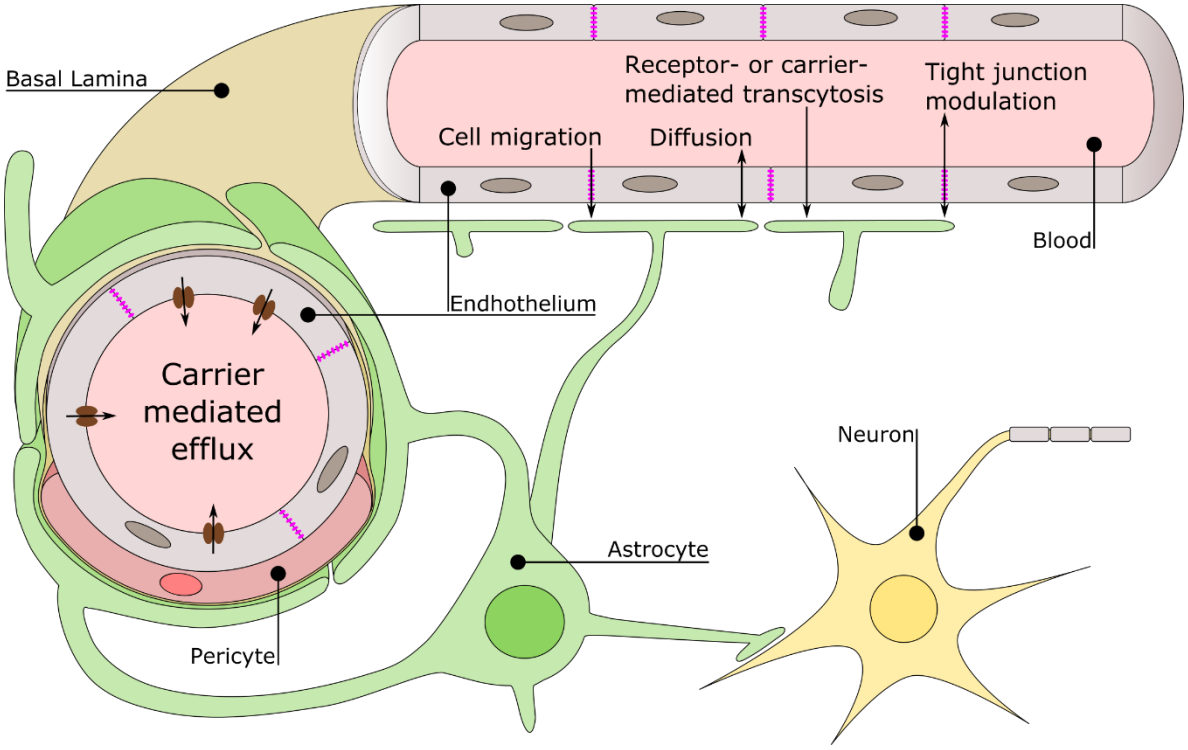

Figure 3. Structure of the BBB, showing the major routes for molecular transport and cell migration through the capillaries into brain tissue (top right), highlighting the route of carrier mediated efflux through the luminal endothelial membrane (left).

Expression of ABC transporters can be different among the species. Out of the several present transporters from the ABC family (e.g. ABCB1, ABCC4 and ABCG2) in the rodent brain, the ABCB1 sub-family encoding P-glycoproteins (P-gp) is the most abundant. The expression of P-gp is approximately four times higher than the breast cancer resistance protein (BCRP (ABCG2)) and 12 times higher than multidrug resistance-associated protein 4 (Mrp4 (ABCC4)) in the rat brain *(39)*. This is in contrast to human tissue where BCRP showed higher expression *(40)*. Differences in BBB penetration of a radioligand between animal models and human measurements might have the most detrimental impact on application of translational results and consequently on the usefulness and predictive value of small animal models in drug development.

1.5.2 Neuroinflammation

Recent studies indicate that neuroinflammation is playing an important role in the pathogenesis of depression, Alzheimer's disease, Parkinson's disease, Huntington's disease and even multiple sclerosis *(41)*, while being one of the main components in the pathophysiological process of brain damage after cerebral ischemia *(42)*.

Microglia is the first cell type to respond to brain damage during neuroinflammation. They are resident macrophages with monocytic origin and their role is to sense CNS injury, remove cellular debris by phagocytosis, astrogliosis regulation or even to assist in the development of CNS *(43)*. As a general process, neuroinflammation occurs through the rapid activation of microglia cells, while astrocytes, the secondary cell types involved during brain damage, respond somewhat slower *(44)*. Besides these two major cell types, inflammatory cells from blood and neurons as well have been connected to neuroinflammation regulation *(45)*.

Microglia is formed by infiltrating monocytes as amoeboid cells during the late embryonic and early post-natal period in the brain *(46)*, taking up around 5% to 12% of total cell population within the different areas of the mouse brain *(47)*. Resting microglia cells have ramified processes but after mechanical injury, ischemia or inflammatory signalling it becomes activated by retracting its processes, increasing the size of its soma, while elevating its cytokine, chemokine, and protease production to prepare for phagocytosis and scar formation (Fig. 4). Microglia activation has been connected to the ATP-binding purinergic receptor, P2X7, which proved to be necessary but not the only regulator of activation *(43)*. In the microglia activation model suggested by Monif et al. the P2X7 receptor acts as a sensory checkpoint, where after tissue damage the adenosine triphosphate (ATP) released from neurons, astrocytes or from other microglia, stimulates microglia activation and proliferation through the formation of the P2X7R pore, while it releases various proinflammatory cytokines such as interleukin-1 β (IL-1β) or tumour necrosis factor α (TNFα) to enable a cascade of similar microglial activation resulting in neuroinflammation *(43)*. While such activation normally helps to maintain tissue homeostasis and drives repair processes *(45, 48)*, over-activation can end in neuronal damage and neurodegeneration *(49)*.

Activated microglia shows an upregulated expression of the 18 kDa TSPO protein in the outer mitochondrial membrane *(50)*. This protein shows a complex role from cell growth, proliferation to mitochondrial respiration and apoptosis, with cholesterol metabolism being one of its most well studied functions. Cholesterol transport through the cytosol is mediated by the steroidogenic acute regulatory protein (StAR) stimulating the transport of cholesterol to the mitochondrial outer membrane *(51)*. TSPO together with at least two other subunit, a 32 kDa voltage-dependent anion channel (VDAC) and a 30 kDa adenine nucleotide carrier (ANC) forms a cluster of four to six molecules creating a single pore at the outer and inner mitochondrial membrane contact sites *(52, 53)*. Though TSPO is wildly perceived to possess a major role in steroidogenesis, Bae et al. have shown evidence on TSPO's anti-inflammatory activity as an adaptive response mechanism *(54)*.

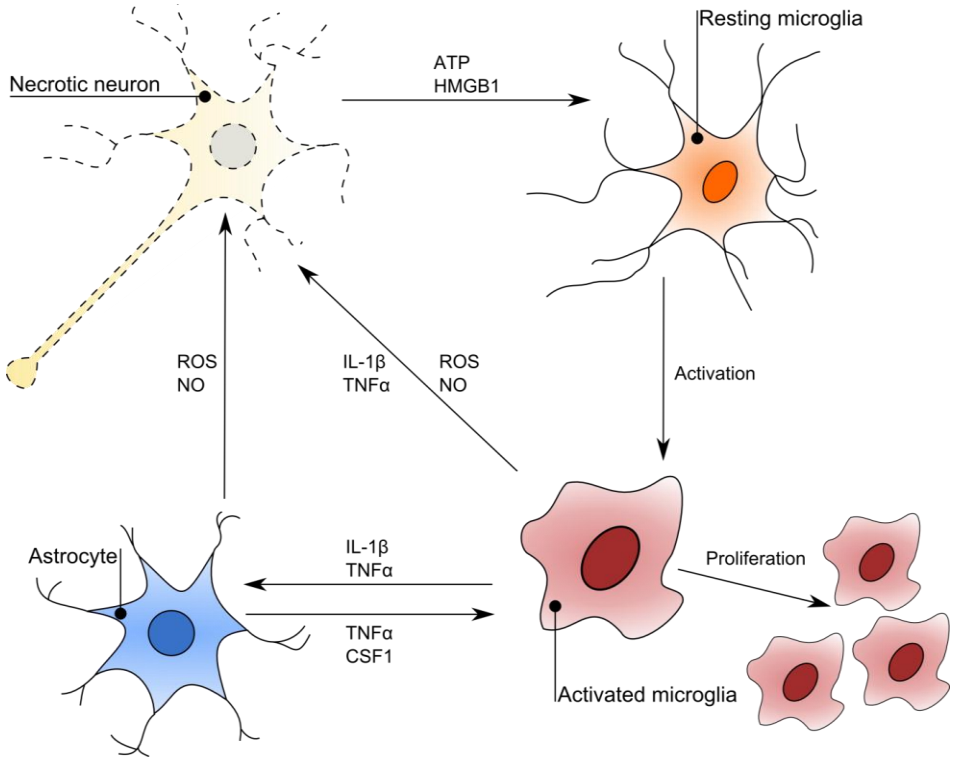

Figure 4. Illustration of the microglia activation and neuroinflammation cascade during neurodegenerative diseases. After tissue damage, the resting microglia changes its shape to activated microglia and activates astrocytes as well with pro-inflammatory mediators as a response to increased level of ATP and high-mobility group box 1 protein (HMGB1) in tissue. Both the astrocytes and activated microglia may produce reactive oxygen species (ROS) and nitric oxide (NO), thereby inducing neurotoxic effects. Further activation and proliferation of microglia is strengthened through astrocytic production of TNFα and colony-stimulating factor 1 (CSF1).

While TSPO is highly expressed in damaged tissue, it is present in the healthy brain only at low levels *(55)*, therefore it has been the main target as a neuroinflammation marker in PET. The search for a TSPO marker resulted in the development of [^{11}C]PK11195 *(56)*. Unfortunately this wildly used TSPO radioligand shows poor signal-to-noise ratio and high non-specific binding *(57)*, therefore many second generation radioligand has been developed such as [^{11}C]PBR28 *(58, 59)*, [^{18}F]FEPPA *(60)*, [^{11}C]DPA-713 and [^{11}C]DPA-714 *(61)*. For this thesis work we have selected the [^{11}C]PBR28 for imaging TSPO, since it has been shown that it has low nonspecific binding and increased signal-to noise ratio compared to [^{11}C]PK11195 *(62)*. In 10% of the human subjects, low affinity binders of TSPO ligands have been identified compared to the normal high affinity binder population *(63, 64)*, while later a third group has been separated as mixed affinity binders with equal distribution of low and high affinity binding sites within one subject *(65)*. The aforementioned variation in binding affinity is due to a single nucleotide polymorphism (rs6971) resulting in one amino-acid change in the TSPO protein *(66)*.

Although the initial observation of increased TSPO in activated microglia in ischemic tissue suggested a selective marker for activated microglia *(67, 68)*, lately it has also been shown in reactive astrocytes around the damaged tissue *(69, 70)*. For this reason TSPO is a complex

cell marker of neuroinflammation, where the signal of TSPO radioligand in brain could originate from both glial cell types.

1.5.3 Phosphodiesterase 10A

The eleven member superfamily of phosphodiesterases (PDEs) consists of more than 20 PDE genes and more than 50 different proteins, which are mainly involved in regulation of signal transduction *(71, 72)*. PDEs are the only enzymes known to degrade cyclic nucleotides, the secondary messenger adenosine and guanosine 3′,5′-cyclic monophosphates (cAMP, cGMP) by hydrolysis to produce AMP and GMP respectively *(73)*. Most PDE families have strict tissue specificity, with specific distribution over the various tissues, cells or even subcellular compartments in brain *(74)*. Due to this selective distribution, the brain can accurately regulate the responsiveness of each tissue to cyclic monophosphate signalling *(75)*.

In the mammalian brain, PDE10A is selectively expressed in the medium spiny neurons of striatum *(76, 77)*. It is capable of hydrolysing both cAMP and cGMP, but has higher affinity for cAMP, therefore cGMP hydrolysis is limited by cAMP activity *(72, 78)*. The GABA-ergic medium spiny neurons are involved in the direct (D_1) and indirect pathways (D_2) of dopamine signalling and activation of both pathways through inhibition of PDE10A function results in lower extrapyramidal side effects while keeping the function of antipsychotic drugs *(79, 80)*. PDE10A has been connected to several basal ganglia related disorders such as bipolar disorder and Parkinson's disease *(81)*, and it is associated also with Huntington's disease (HD) *(82, 83)*. Inhibition of PDE10A is a primary interest in research related to treatment of schizophrenia *(84)*, as they provide possibility to manipulate the intracellular signalling cascades without the side effects of traditional neurotransmitter driven approaches *(78)*.

In order to successfully visualize changes in PDE10A levels *in vivo* several radioligands have been suggested for PET imaging: [^{11}C]papaverine *(85)*, [^{18}F]JNJ41510417 *(86)*, [^{11}C]MP-10 *(87)*, [^{18}F]MNI654, [^{18}F]MNI659 *(88, 89)*, [^{18}F]JNJ42259152 *(90)*, and [^{11}C]AMG 7980 *(91)*. Due to different reasons (low binding potential, short retention time in striatum, need for arterial input function, etc.) neither of these radioligands have proven to be optimal for PDE10A imaging, thus ligand optimization is still an ongoing process.

Several PDE10A knockout mice strains have been characterized to reveal the function of PDE10A in behavioural studies and to help the biomarker development. Availability of knockout animal strains is an advantage for identifying a selective function of a gene. One of the earliest PDE10A-/- mice was developed on DBA1LacJ background which was later transferred to a C57/Bl6N background *(92)*. Both the C57/Bl6N and DBA1LacJ background knockout animals show decrease in exploratory locomotor activity, learning delay during conditioned avoidance responding task while maintaining equivalent levels of striatal cAMP or cGMP compared to wild type animals. Effects on the dopaminergic system appear to be background-dependent and observed on C57BL6N mice only *(93)*.

Another PDE10A knockout mouse model has been developed specifically as a PDE10A2 spliceform knockout on the C57BL6 background. While PDE10A1 is the specific spliceform of PDE10A in the testis, PDE10A2 is selective for the medium spiny neurons in the striatum *(78, 94)*. The PDE10A2-/- mouse model does not show significant decrease on locomotor activity, but an increase in social interest towards other mice, providing a connection between the effects of PDE10A2 on cAMP signalling and social interaction *(94)*.

2 AIMS

The overall aim of the present thesis was to facilitate improvements and to develop novel methodological platforms for small animal imaging PET. The specific aims were the following:

- To validate a multimodal imaging system specifically designed for rodent and small animal imaging.
- To present the importance of animal model selection in PET translational research.
- To offer quantification method for the neuroinflammation marker [^{11}C]PBR28 in a longitudinal setup.
- To validate a new stroke animal model for small animal research.
- To validate a novel radioligand for PDE10A imaging.

3 MATERIALS AND METHODS

The present chapter is a summary of the general methods used during this thesis work.

3.1 ANIMALS

All animals were acquired from Charles River Laboratories (Sulzfeld, Germany) and only male animals were included in the experiments, the different strains used in each study are summarized in Table 1. Every animal had at least 1 week resting period before the start of experiments to habituate to its new environment. Animals were housed in groups according to regulations at Karolinska Institutet in a thermoregulated (~ 22°C) and humidity-controlled facility under a 12 h/12 h light/dark cycle with access to food and water ad libitum.

Table 1. The different mouse, rat and guinea pig strains used in this thesis work.

	Mouse	**Rat**	**Guinea pig**
Study I	C57BL/6J	Wistar	-
Study II	C57BL/6J	Wistar	Dunkin Hartley
Study III	C57BL/6J	Wistar	-
Study IV	-	Sprague-Dawley	-
Study V	B6.D1-de10a<tm1Pfi>/J and C57BL/6J	-	-

All animals in Study I, II and III were wild type animals.

In study II supplement, we present results from multidrug resistance protein 1a (MDR1a) knockout rats. In rodents the Mdr1 gene has two subtypes Mdr1a, the equivalent of the human P-gp, and Mdr1b. Mdr1a is expressed mostly in the BBB, intestine and blood-testis barriers, while Mdr1b is found in brain parenchyma, kidney and liver. By specifically removing the function of Mdr1a (P-gp), it is possible to visualize the effect of P-gp on brain.

In study IV we have used a surgically induced ischemic stroke model in Sprague-Dawley rats; these animals went through an occlusion of the M2-segment of the left middle cerebral artery (M2CAO) before imaging.

3.1.1 Ethical approval

All animal experiments were conducted according to the guidelines of the Swedish National Board of Laboratory under protocols approved by the Ethics Review Board of Northern Stockholm, Sweden (N210/10; N557/11; N253/12; N40/11).

3.2 RADIOCHEMISTRY

The following radioligands have been used in this thesis: [^{11}C]AZ10419369, [^{11}C]PBR28, [^{11}C]T-773, [^{11}C]FLB 457. All of them were prepared at Karolinska Institutet with methylation of their respective desmethyl precursor using [^{11}C] methyl triflate.

Preparation of [^{11}C]AZ10419369 was according to procedures described earlier in detail *(95, 96)*, while [^{11}C]PBR28 was synthesized similarly to previously described methods with partial modifications *(97)*. [^{11}C]T-773 and [^{11}C]FLB 457 was labelled by an O-methylation reaction according to previously reported methods *(98, 99)*. In short, radioligand preparation was done by the following procedures: [^{11}C]CH_4 was released from the target and collected in a Porapak Q trap cooled with liquid nitrogen. Following the collection [^{11}C]CH_4 was released from the trap by heating with pressurized air and subsequently [^{11}C]CH_4 was mixed with vapours from iodine crystals at 60°C, directly followed by a radical reaction at 720°C. After the reaction, [^{11}C]CH_3I was collected in a Porapak Q trap at room temperature and the unreacted [^{11}C]CH_4 was recirculated for another 3 min. The Porapak Q trap was heated to 180°C by a home-produced oven to release [^{11}C]CH_3I from the trap. [^{11}C]methyl triflate was prepared by sweeping [^{11}C]CH_3I vapour through a heated glass column containing silver-triflate-impregnated graphitized carbon.

The radiosynthesis of each radioligand was obtained by trapping [^{11}C]methyl triflate at room temperature in a reaction vessel containing the corresponding mixture of precursor, base and solvent. After the reaction, the respective mixture was diluted with HPLC eluent before being injected to the HPLC system to purify the product. Afterwards the ligands were formulated in 10% EtOH/PBS mixture.

3.3 EXPERIMENTAL DRUGS:

3.3.1 Cyclosporin A

Cyclosporin A (CsA) is an immunosuppressive drug used in organ transplantation. Due to its nonsteroidal nature it doesn't have bone marrow suppression (myelotoxicity) which is a major advantage in clinical use *(100)*. CsA inhibits promoters of T-cell activation to reduce immune response, inhibits lymphokine production and the release of interleukins leading to reduced T helper cell (adaptive immune system) activity *(101)*.

It has been found, that CsA uptake in the brain is restricted by P-glycoprotein (P-gp (ABCB1)) an efflux pump in the endothelial cells of the brain capillaries *(102)* and that CsA has the potential to enhance the accumulation of chemotherapeutic agents through the BBB into brain tissue *(103)*. Therefore CsA has been recognized as an inhibitor of P-gp function and has been used as a P-gp blocker in PET experiments *(104)*. Recently it has been recognized that CsA is not selective for P-gp but it has varying affinity for many transport proteins from the solute carrier family, such as other ABC transporters like mrp2 (ABCC2) and BCRP or different organic anion-transporting polypeptide (OATP) transporters as well *(105–108)*.

In Study II 50 mg/ml CsA (formulated in 96% ethanol) was administered intravenously 15 min before the injection of the radioligand. CsA was purchased from Novartis Sverige AB (Täby, Sweden). Due to the side effects of CsA (nephrotoxicity, neurotoxicity, hypertension etc.), the animals were terminated right after the experiments with CsA pretreatment.

3.4 PHANTOMS USED FOR PHYSICAL VALIDATION

3.4.1 PET

For spatial resolution and sensitivity measurements, we used a 370 kBq 22Na point source (MMS09-022-10U; Eckert and Ziegler). The source is embedded into a 1 cm^3 acrylic cube. Since iterative algorithms can overestimate the resolution of point sources in air *(109)*, spatial resolution achievable in preclinical studies was evaluated using a micro-Derenzo phantom.

Scatter fraction, count losses, and random coincidence measurements were performed with the mouselike (70 mm length, 25 mm diameter) and ratlike (150 mm length, 50 mm diameter) phantoms, consisting of a high-density polyethylene cylinder with an off-centred axial bore of 3.2 mm diameter for a plastic tube filled with $^{18}F^-$ ions in rinse water.

For image quality, accuracy of attenuation, and scatter corrections we have used the NEMA NU 4 image quality phantom filled with [^{18}F]FDG.

3.4.2 MR

To measure the signal-to-noise ratio and image uniformity we used a plastic sphere 46 mm in inner diameter and a cylinder 21 mm in inner diameter and 60 mm in length. Both phantoms were filled with the same solution of $NiCl_2$, having T_1 and T_2 relaxation times of 129 and 125 ms, respectively.

For the 2D geometric distortion and geometric fidelity measurements the test object was a sphere of 46 mm inner diameter with a cube inside and filled with a dilute solution of NiCl2.

3.5 IN VIVO PET EXPERIMENTS

In all experiments with PET the animals were anaesthetized under isofluorane gas anaesthesia (induction: 4% - 5%, maintenance 1.5% - 2%) and placed into a heated imaging chamber with inbuilt temperature and breathing monitoring. The head was fixated through the mouth cone of the bed and the whole body of the animal was covered and taped to the imaging chamber for insulation and movement restriction during multimodal imaging. Before the PET experiments a cannula was inserted in the tail vein of the mice and rats, and in case of the guinea pigs in the tarsal vein for ligand injection.

3.5.1 PET systems

During this thesis work the Mediso nanoScan PET/MRI and nanoScan PET/CT small animal imaging systems were used (Fig. 5). Both systems are based on identical PET rings consisting 12 detector modules of lutetium yttrium orthosilicate:cerium (LYSO:Ce) crystals and 2

multianode position-sensitive photomultipliers (H9500; Hamamatsu) per detector module *(110)*.

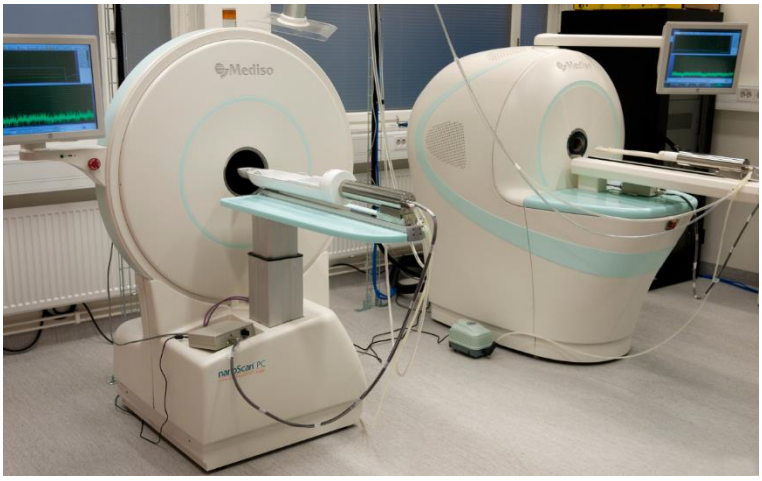

Figure 5. Mediso nanoScan PET/CT (on the left) and nanoScan PET/MRI (on the right) small animal imaging systems installed at KI PET Center.

3.5.2 PET experimental procedures

The animals were positioned in the PET camera in transaxial position with their heads in the center of the FOV. Before each injection, the radioligand was diluted in saline to reach around 60-100 MBq/ml solution in case of rats and guinea pigs and 100-150 MBq/ml in case of mice. The aimed volume of diluted radioligand for injection was 0.1 - 0.2 ml in mice and 0.3 - 0.5 ml in rats and guinea pigs in line with the guidelines of bolus injection for small animals. The injected volume was adjusted based on the weight of the animal. The radioligand was intravenously administered simultaneously with the start of the PET acquisition and was followed by a 0.1 ml saline flush in mice and 0.2 ml in rats and guinea pigs.

During the PET measurements radioactivity levels in the brain were measured continuously using the Mediso nanoScan PET/MRI and the nanoScan PET/CT small animal imaging systems in list mode. Two animals were examined at the same time in the identical PET modules of the two PET systems. The acquired data was later reconstructed into different timeframes depending on acquisition length. With 63 min long scans we have used 25 timeframes (consisting 4x10 s, 4x20 s, 4x60 s, 7x180 s, 6x360 s frames) in case of mice and rats in Study I-V, while with 93 min long scans we have used a 35 timeframe setup (consisting 4x10 s, 4x20 s, 4x60 s, 7x180 s, 11x360 s frames) in case of guinea pigs in Study II. For reconstruction a fully 3-dimensional MLEM algorithm was applied with 20 iterations, without the use of scatter and attenuation correction.

3.5.3 Radiometabolite determination in plasma

In Study III we have used reversed-phase HPLC methods to evaluate metabolism of [^{11}C]PBR28 in rats by determining the percentage of radioactivity in plasma that corresponded to the unchanged radioligand and its radioactive metabolites during our

experiments. During these experiments, four rats have been prepared with a second cannula in the femoral artery for blood sampling in addition to the cannula in their tail vein for radioligand injection. Sixteen arterial blood samples of 0.1 ml were taken for measurement of radioactivity in plasma and blood using a gamma counter and four samples of 0.5 ml blood were taken for radiometabolite analysis at 4, 20, 40 and 60 minutes after injection.

For the metabolite analysis plasma was obtained by centrifugation of 0.5 ml blood at 2000 g for 2-4 min. The plasma was mixed with acetonitrile (0.35 ml) afterwards and centrifuged for another 4 min. The supernatant was mixed with 2 ml of water and injected to a HPLC system for analysis. Peaks for radioactive compounds eluting from the column were integrated and the unchanged radioligand was expressed as a percentage of the sum of the areas of all detected radioactive compounds (decay-corrected to the time of injection on the HPLC).

3.5.4 Regions of interests and brain templates

The reconstructed dynamic mouse and rat PET images in study I-V were co-registered to their respective MRI template available in PMOD incorporating volume of interest (VOI) sets as well (PMOD Technologies Ltd., Zurich, version: 3.3). Coregistration was done manually with the use of mean PET images focusing on early (flow phase) and late (binding phase) PET signals. In study II the guinea pig scans were coregistered to a template MRI with an in-house developed VOI set using similar procedures as with mice and rats (Fig. 6).

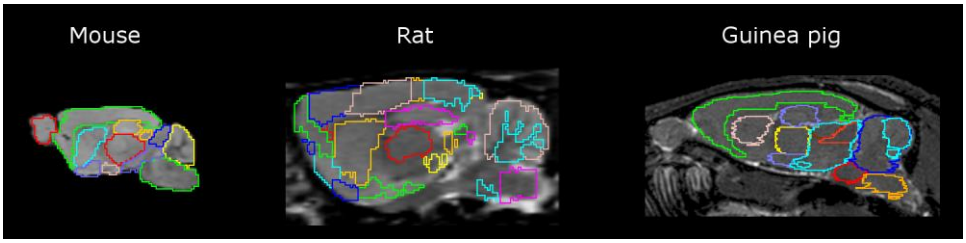

Figure 6. Mouse, rat and guinea pig regional VOIs overlaid on a sagittal section of their respective MRI template.

With the help of these VOI sets, decay corrected time activity curves (TAC) were generated. Whole brain and regional brain uptake values were expressed as percent standard uptake value (%SUV), which was calculated by normalizing regional radioactivity for injected radioactivity and body weight (Fig. 7).

$$\%SUV(t) = \frac{\text{tissue radioactivity concentration(t)}}{\text{injected radioactivity}(t_0)/\text{body weight}} \text{x } 100$$

Figure 7. Calculation of percent standard uptake value (%SUV).

3.5.5 Quantitative PET data analysis

In this thesis Logan Graphical Analysis and 2-TCM has been used to calculate V_T of [^{11}C]PBR28 (Study III) and SRTM modelling was used to estimate BP_{ND} of [^{11}C]AZ10419369 (Study II) or [^{11}C]T-773 (Study IV).

3.6 SURGICAL PROCEDURES - M2CAO

The animals were placed into an interventional angiography system (Philips AlluraXper XD, Philips Medical Systems, Best, The Netherlands) and anaesthetized with inhalation of isoflurane (1.5% in oxygen) during surgery. A microwire (0.007F Hybrid Microwire; Balt Extrusion, Montmorency, France) sheeted within a microcatheter (1.5F hydrophilic Ultraflow; Covidien, Mansfield, MA, USA) was introduced through the ventral tail artery and the tip was navigated to the M2-segment of the left middle cerebral artery creating occlusion of the artery (M2CAO). After 90 minutes the microwire was removed *(111)*.

3.7 IMMUNOFLUORESCENCE STUDIES

In Study IV, parallel to PET, immunofluorescence (IF) techniques were used to outline the cellular response to acute ischemic injury following M2CAO.

After sacrificing the animals all brains were snap frozen and kept at -80°C until cryosectioned at 14 μm thickness. Samples were collected after 1, 2, 3, 4, 7, 14 and 22 days after reperfusion. The sections were triple stained with anti-Cd11b (marker for monocytes/macrophages and microglia), glial fibrillary acidic protein (GFAP, marking astrocytes and ependymal cells) and TSPO antibody according to a standard IF protocol and tyramide signal amplification (TSA) technique *(112)*. On separate slices neuronal nuclei marker was used for lesion delineation, in combination with phagocyte marker anti-Cd68 in a double staining regime *(113)*.

Cd11b/GFAP/anti-TSPO Triple staining data set: Sections were scanned on a Vslide slide scanning microscope (Metasystems, Altlußheim, Germany) and the images were analysed in Metaviewer software (Metasystems). For confocal laser microscopy, images were captured on a Zeiss 710LSM laser-scanning microscope. Cells were registered as positive if meeting the following criteria: clear antibody immunoreactivity and positive for nuclear counterstaining. Weak or dispersed staining patterns were considered negative.

4 RESULTS AND DISCUSSION

4.1 OVERVIEW

This thesis focuses on advancements in the small animal imaging field with PET. Most of the obstacles in small animal imaging revolve around the subject's relatively small size and the fact that some of the methodologies used routinely in human PET are not easily applied to rodents. The aim was to improve on several aspects of small animal imaging, starting with a development of a high resolution small animal PET system (Study I), to bring attention to the importance of species selection in PET translational research (Study II) and to overcome the obstacle of limited available blood volumes for metabolite analysis in longitudinal experiments (Study III). Finally said advancements have been applied during the validation of a neuroinflammation animal model (Study IV) and in the development of a new PET ligand (Study V).

4.2 SECTION 1 - SCANNER PHYSICAL VALIDATION

4.2.1 Study I: Validation of the nanoScan PET/MRI system

The nanoScan PET/MRI is a high-resolution integrated system for consecutive PET and MR imaging of small laboratory animals. The imaging system uses magnetically shielded position-sensitive photomultiplier tubes together with a compact 1 Tesla permanent-magnet MRI. We evaluated the performance of the system, using different NEMA standards (PET: NEMA NU 4-2008; MRI: NEMA MS 1-2007, MS 2-2008 and MS 3-2007) to measure spatial resolution, sensitivity, counting rate capabilities, and image quality parameters. Finally we have complemented our test with several in vivo experiments to demonstrate the systems real-life performance.

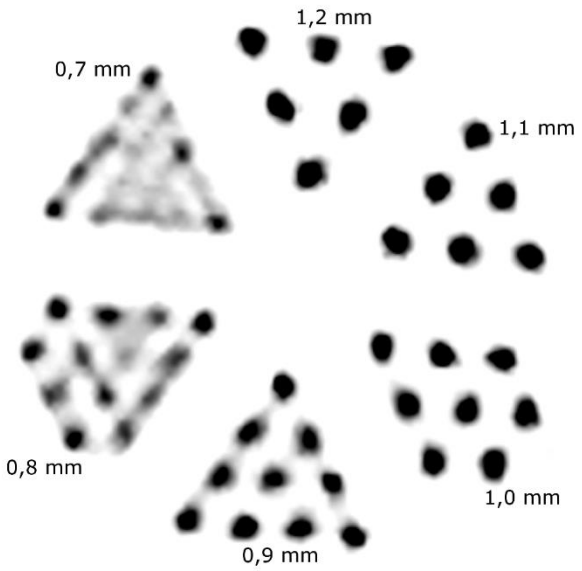

Figure 8. Image of a micro-Derenzo phantom filled with 9.34 MBq of [^{18}F]FDG. Diameters of rods within the sections are 1.2, 1.1, 1.0, 0.9, 0.8 and 0.7 mm.

The spatial resolution of the PET system enabled the 0.8 mm rods of a Derenzo phantom to be resolved (Fig. 8). With point source and 2-dimensional filtered back-projection reconstruction, the resolution varied from 1.50 to 2.01 mm in full width at half maximum in the radial direction and from 1.32 to 1.65 mm in the tangential direction within the radius of 25 mm.

The performance characteristics of the PET system were comparable to the previous validation of nanoScan PET/CT *(110)*, therefore the system proved to be not compromised as a result of their integration onto a single platform. During the testing of the MR imaging component, we have acquired artefact-free images with high signal-to-noise ratio (Fig. 9). Geometric distortion was below 5%, and image uniformity was at least 94.5% and 96.6% for the 60 and 35 mm radiofrequency coils, respectively.

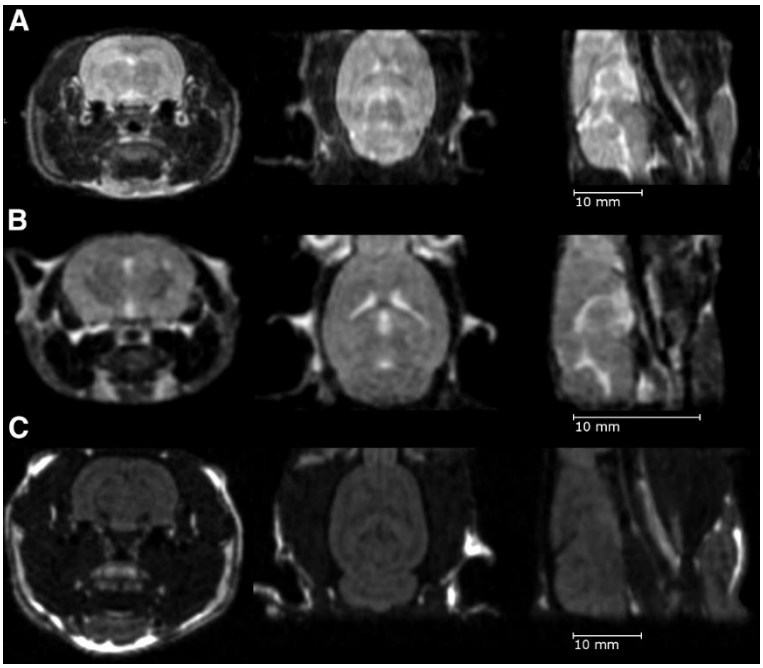

Figure 9. Three-dimensional MR brain scans: T2-weighted fast spin echo in rat, with scan time of 22:24 min (A); T2-weighted fast spin echo in mouse, with scan time of 20:00 min (B); and spoiled gradient echo in rat, with scan time of 14:13 min (C).

Due to the combination of features and performance parameters in the nanoScan PET/MR imaging system, we now have the possibility to use a multimodal system, with anatomical information on soft tissue together with functional images from PET to improve our small animal imaging analysis.

4.3 SECTION 2 - METHODOLOGICAL CHALLENGES IN SMALL ANIMAL IMAGING

4.3.1 Study II: Species differences in blood-brain barrier function

The main objective of the present study was to explore the differences in BBB transport of [^{11}C]AZ10419369, with special regard to the ABC transporter activities, in three rodent species: mouse, rat and guinea pig. PET measurements were performed after i.v. injection of [^{11}C]AZ10419369 in the baseline conditions and after pretreatment with cyclosporin A (CsA), an inhibitor of ABC transporters. In the study we have imaged eight male C57BL/6J mice, seven male Wistar rats and seven male Dunkin Hartley guinea pigs under baseline conditions and, on separate experimental days, 15 min after administration of 50 mg/kg CsA. Uptake values (%SUV) were calculated as a summation of uptake from 10 min to the end of the PET acquisition and non-displaceable binding potential (BP_{ND}) was estimated using SRTM *(13)*.

During baseline conditions the brain uptake was low in mice and rats with fast clearance of [^{11}C]AZ10419369, while there was a slow wash out in guinea pigs in both conditions (Fig. 10). After CsA pretreatment the peak whole brain uptake values of [^{11}C]AZ10419369 increased by 207% in mice, 94% in rats and 157% in guinea pigs. The highest BP_{ND} values were obtained in the striatum and thalamus ($BP_{ND} \approx 0.4$) in mice after CsA pretreatment, while in rats the highest binding areas were the striatum, thalamus, hypothalamus and periaqueductal grey ($BP_{ND} \approx 0.5$). In guinea pigs we did not find any significant changes in BP_{ND} between baseline and CsA pretreatment, except in the striatum, which was probably due to the remarkably slow wash out. In most of the guinea pig measurements neither of the regions could reach equilibrium despite the 2 hour long scanning time, which makes the SRTM calculations unreliable.

The difference in kinetics and BP_{ND} observed in guinea pigs, compared with mice and rats, is most likely due to the differences in homology of the 5-HT$_{1B}$ receptor and the affinity of [^{11}C]AZ10419369 to the 5-HT$_{1B}$ receptor. A previous report indicated that amino acid residue 335 in the 5-HT$_{1B}$ receptor is a major determinant of its reactivity with several ligands *(114)*. It has also been shown that AZ10419369 binds to human (K_i = 0.8 nM) and guinea pig (K_i = 0.01 nM) 5-HT$_{1B}$ receptors with higher affinity than it does to rat 5-HT$_{1B}$ receptors (K_i = 2.3 nM) *(95)*.

These results indicate that BBB penetration of [^{11}C]AZ10419369 was hindered by ABC transporter activity in all three species, which highlights the importance of ABC transporters in the design of pre-clinical PET studies and during evaluation of results in translational research.

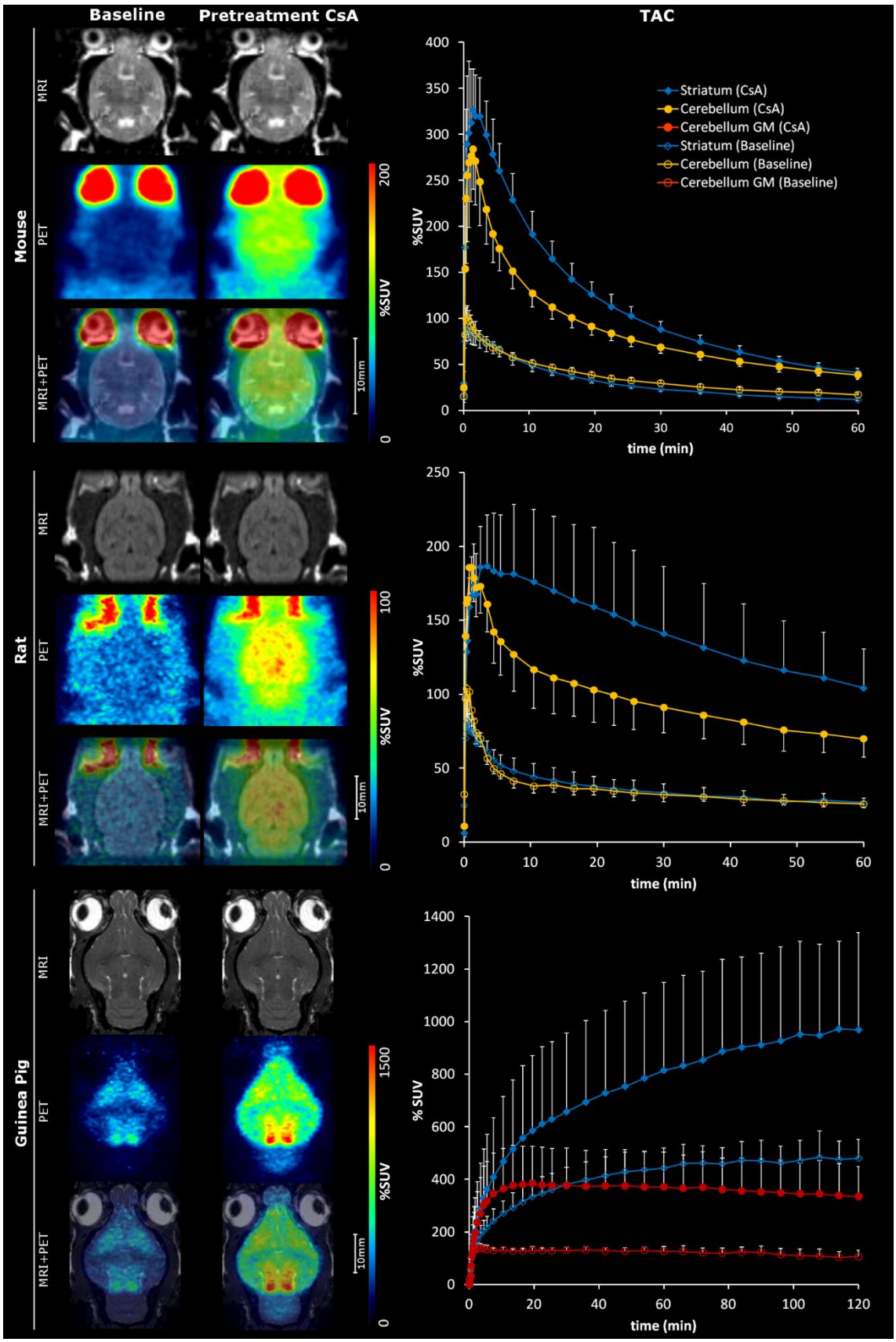

Figure 10. Representative %SUV uptake images from 10 min until the end of the scan (total 53 min in case of rat and mice, 113 min in case of guinea pig) on the left, while time activity curves of striatal and cerebellar uptake are presented on the right as mean values and SD as error bars, in mouse (n = 8), rat (n = 7) and guinea pig (n = 7) in baseline and pretreatment condition.

4.3.2 Study III: Validation of %SUV as an outcome measure for [^{11}C]PBR28 imaging in rodents

Quantification of radioligands without a reference region in rodents, especially in mice, is quite difficult. The small amount of blood in rodents challenges our techniques for blood sampling, while in longitudinal studies the use of plasma-derived input for quantitative measurements seems impossible. Molecular imaging of TSPO, a marker for neuroinflammation, with [^{11}C]PBR28 holds these difficulties, due to the absence of a standard reference region in the brain. The aim of this study was therefore to evaluate the use of the standardized uptake value (SUV) as an outcome measure for TSPO imaging with [^{11}C]PBR28.

To achieve this we have used four healthy male Wistar rats to determine the correlation between the V_T and SUV. In a separate group of four healthy male Wistar rats and four healthy male C57BL/6J mice we have determined the test-retest variability of the SUV (Fig. 11).

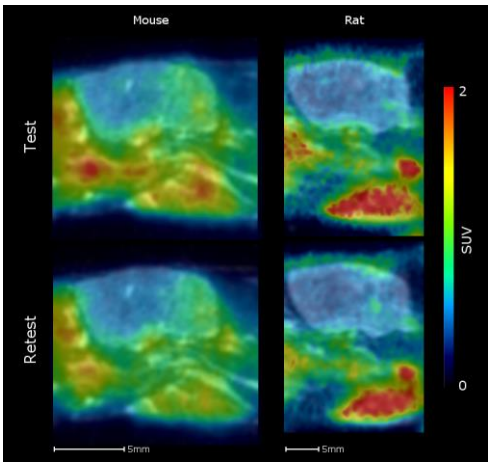

Figure 11. Sagittal test-retest PET images of a representative mouse and rat experiment are shown overlaying the individual MRI measurements.

The whole brain V_T of [^{11}C]PBR28 in rats was 43.1 (Logan) and 47.3 (2-TCM), with a very high correlation of V_T values obtained from 2-TCM and Logan analysis for the eight different brain regions. There was a statistically significant correlation ($r^2 = 0.94$; $p < 0.001$ with Logan; $r^2 = 0.92$; $p < 0.001$ with 2-TCM) between the V_T and the SUV of 8 brain regions (Fig. 12).

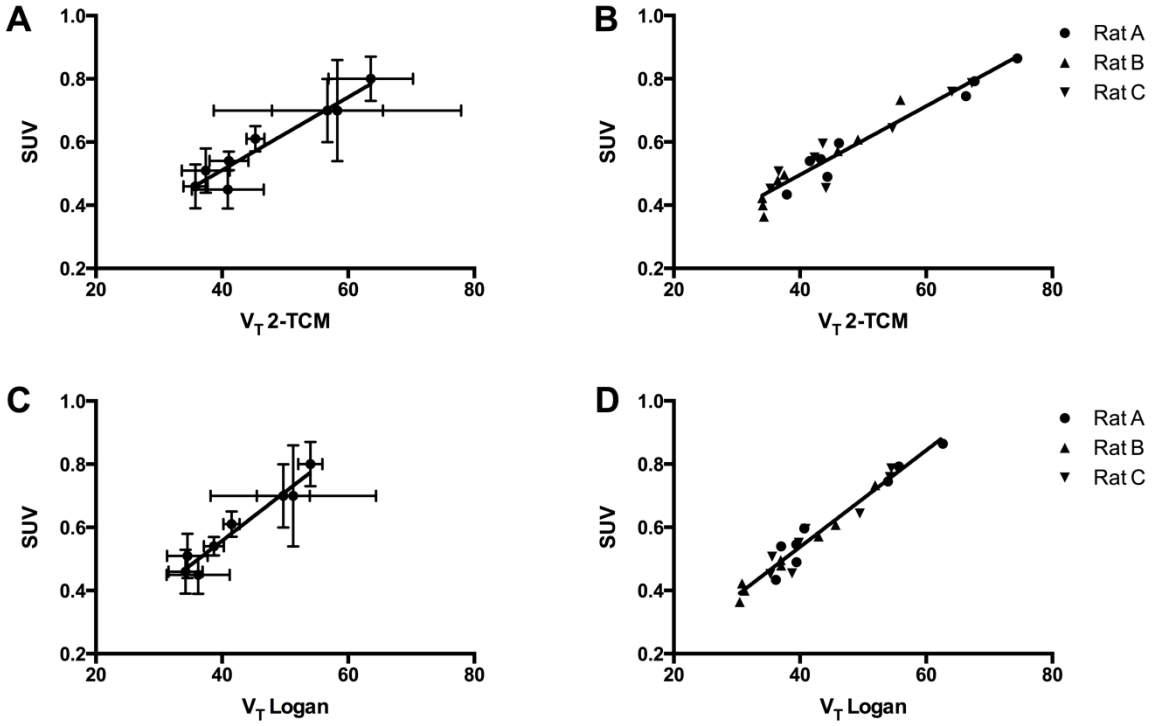

Figure 12. Correlation between V_T of [^{11}C]PBR28 as calculated using two-tissue compartment modelling (2-TCM) (A+B) and Logan graphical analysis (C+D), and the SUV of [^{11}C]PBR28, for the averages of eight brain regions (A+C) and for the individual values for each rats for the eight brain regions (B+D).

The test-retest variability of SUV in 8 brain region ranged from 8% to 20% in rats and from 7% to 24% in mice (Table 2).

Table 2. Test-retest variability (TRV) of [^{11}C]PBR28 for rats and mice.

	TRV in rats	**TRV in mice**
Striatum	13.6 ± 4.8	23.6 ± 15.6
Hippocampus	7.7 ± 3.5	6.9 ± 4.7
Hypothalamus	20.4 ± 15.4	23.0 ± 17.6
Midbrain	12.3 ± 15.8	15.1 ± 6.3
Thalamus	13.7 ± 9.2	7.6 ± 4.6
Cerebral cortex	16.7 ± 9.2	13.4 ± 11.6
Brainstem	17.7 ± 7.8	13.2 ± 9.1
Cerebellum	11.5 ± 7.4	13.7 ± 6.4

Validation of SUV as an outcome measure for [^{11}C]PBR28 imaging in rodents was an important step in order to show that SUV can be used as an outcome measure in subsequent longitudinal small animal PET studies.

4.4 SECTION 3 - APPLICATION OF ANIMAL MODELS

4.4.1 Study IV: Validation of a neuroinflammation animal model

Adequate estimation of neuroinflammatory processes following ischemic stroke is essential for our better understanding of disease mechanisms and for the development of treatment strategies. With [^{11}C]PBR28, we monitored longitudinally the inflammatory response post transient cerebral ischemia in rats, using a recently developed rat stroke model that produces isolated focal cortical infarcts with clinical relevance in size and pathophysiology. Six Sprague-Dawley rats went through a 90 min transient endovascular occlusion of the M2 segment of the middle cerebral artery (M2CAO). Animals were imaged with 1, 4, 7 and 14 days after M2CAO with a bolus injection of [^{11}C]PBR28.

In the infarct region we found a significantly increased uptake of [^{11}C]PBR28 on day 4, 7 and 14 compared to day 1 as well as compared to the contralateral cortex (Fig. 13). No significant difference was detected in the contralateral cortex during the 14 days of imaging. The activation in the infarct region gradually decreased between day 4 and day 14.

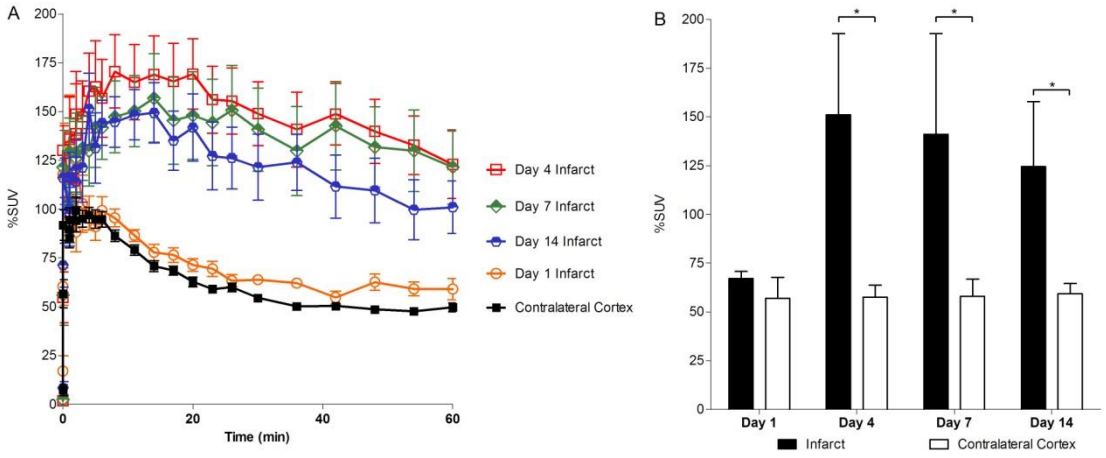

Figure 13. (A) Average time activity curves of infarct areas on day 1(n = 6), day 4 (n = 6), day 7 (n = 6) and day 14 (n = 5) and contralateral cortical areas from all imaging days (n = 23). (B) %SUV values of [11C]PBR28 uptake in the Infarct and the Contralateral Cortex region on day 1 (n = 6), day 4 (n = 6), day 7 (n = 6) and day14 (n = 5) (* = $p < 0.05$).

In an additional group of animals (n = 26), immunofluorescence studies were performed with antibodies for activated microglia/macrophages (Cd11b, Cd68), astrocytes (GFAP) and TSPO. The TSPO immunofluorescence signal indicated reactive microgliosis post injury, corresponding to the PET findings.

Based on the findings the present M2CAO animal model together with [^{11}C]PBR28 appears to be well suited for studies on neuroinflammation after ischemic stroke.

4.4.2 Study V: Molecular imaging of PDE10A - Radioligand validation in knockout mice

The development of PDE10A-selective PET radioligands is of high importance as they can serve as molecular imaging biomarkers in the development of therapeutic drugs, help during the diagnosis of different neurological or psychiatric diseases such as HD, and also allow for monitoring the therapeutic effect of drugs in HD patients. Knockout animals offer an excellent advantage for radioligand development due to their added value of dissecting the specific signal from non-specific sources. In this study we have evaluated the newly developed radioligand [^{11}C]T-773 in PDE10A knockout mice (heterozygous[HET] and homozygous [HOM] B6.D1-Pde10a<tm1Pfi>/J) and used wild type animals (WILD, C57BL/6J) as controls.

[^{11}C]T-773 showed accumulation in the striatum over time, whereas in other brain regions examined (i.e., cerebellum and cortex), there was a clear rapid washout. There was an acceptable uptake in the striatum of WILD mice, moderate uptake in HET mice, and low uptake in HOM mice (Fig. 14).

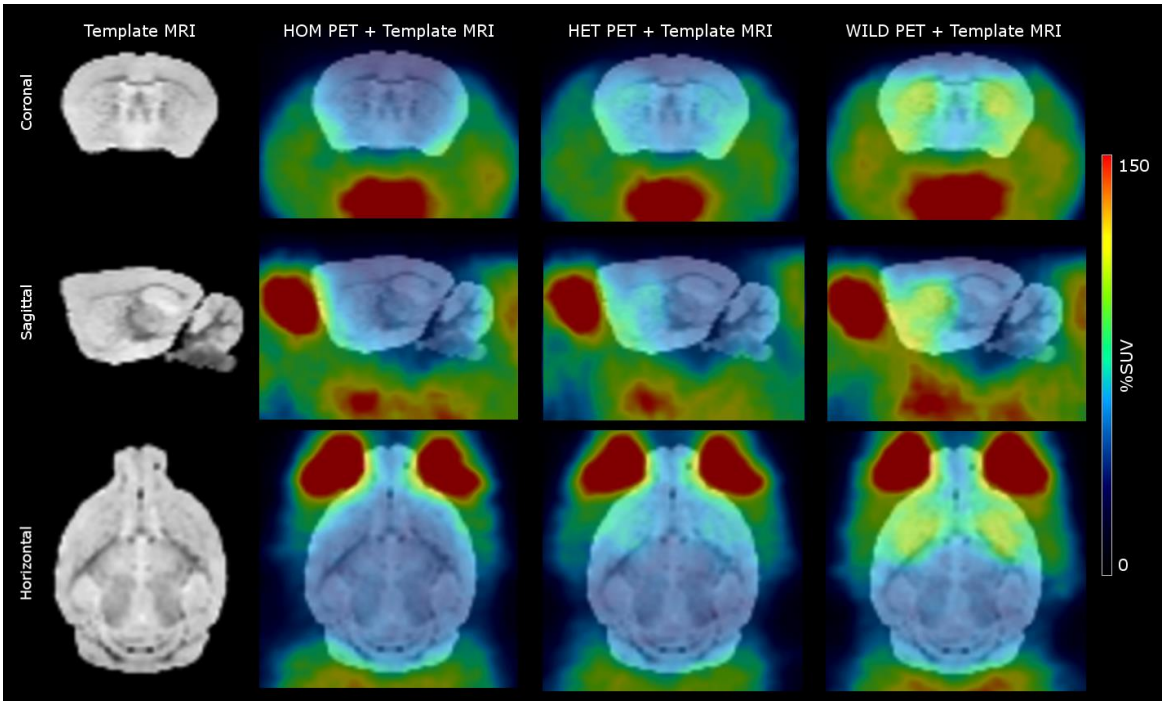

Figure 14. Representative images of [^{11}C]T-773 uptake (summation of 15-63 min) in homozygous (HOM), heterozygous (HET) and wild-type (WILD) mice (from left to right) overlayed on mice template MRI (left).

Based on %SUV values (15-63 min) the uptake of radioligand in the striatum of HOM mice was 44% lower while 25% lower in HET mice compared to WILD mice. Between each animal group the striatal %SUV values were significantly different ($p < 0.0001$) and the BP_{ND} values were significantly lower in homozygous and heterozygous animals compared to WILD ($p < 0.0001$) (Fig. 15).

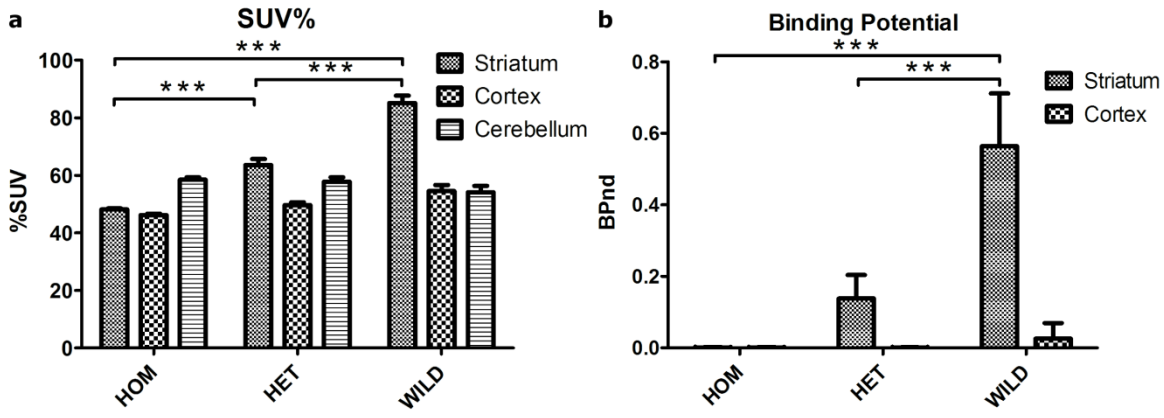

Figure 15. Comparison of %SUV in Striatum, Cortex and Cerebellum (a) and BP_{ND} in Striatum and Cortex (b). Values are means ± SD.

The significant reduction of binding in the striatum in PDE10A knockout mice confirms that [^{11}C]T-773 binds selectively to PDE10A, and the clear regional distribution of uptake strengthens the suitability of [^{11}C]T-773 as a radioligand for imaging PDE10A.

5 CONCLUSIONS

The findings of the present thesis, focusing on methodological advancements in the small animal PET imaging field, are summarized below.

5.1 SECTION 1

- Combination of a 1 Tesla standard MRI magnet with the PET ring of the nanoScan PET/CT system did not affect the performance of the final nanoScan PET/MRI system. Together with the integrated MRI component the system is capable of conducting consecutive multimodal imaging with functional images from PET and provides anatomical information on soft tissue while keeping the subject animal in the same position. Indicating that combined PET-MRI systems have a great advantage in pre-clinical imaging, due to their improved work-flow performance as compared to that of stand-alone systems.

5.2 SECTION 2

- ABC transporter activity in translational research should be taken into account as the BBB penetration of [^{11}C]AZ10419369 was completely blocked in mouse and rat while only reduced in guinea pig. This highlights the necessity of proper animal model selection while designing pre-clinical PET studies.
- SUV can be used as an outcome measure for [^{11}C]PBR28 imaging in rodents in longitudinal small animal PET studies, as the validation of [^{11}C]PBR28 test-retest in healthy mice and rats showed good results and there was a statistically significant correlation between V_T and SUV of [^{11}C]PBR28 in rats.

5.3 SECTION 3

- The M2CAO stroke rat model showed significantly up-regulated TSPO signal, measured with [^{11}C]PBR28, in the infarct region. There was a decrease of said activation from day 4. showing that the present M2CAO model is well suited for studies on neuroinflammation with a more rapid response compared to the previous MCAO model.
- The significant reduction of binding in the striatum in PDE10A knockout mice confirms that [^{11}C]T-773 binds selectively to PDE10A, and the clear regional distribution of uptake strengthens the suitability of the ligand.

6 FUTURE PERSPECTIVES

Improvements on MRI based attenuation maps

One limitation of combined PET/MRI imaging compared to PET/CT systems is the lack of readily available attenuation maps. Even though this is less of an issue in small animal brain imaging, where the head is not subject to movement and the thin skull of rodents is equally distributed around the brain, other research areas like lung or hearth imaging could greatly benefit from the same level of attenuation and scatter correction as in PET/CT systems.

Image derived input function

Even though SUV has proven to be applicable for [^{11}C]PBR28 uptake estimation in rodents, for other radioligands without reference region in the brain the same might not be possible. Small animal imaging has the possibility of simultaneous brain and hearth imaging due to the large FOV compared to the body size of some rodent species. This has the possibility to facilitate the application of image derived input function methods similar to the advancements in human research *(115)*, but with the use of the left ventricle instead.

New neuroinflammation marker

As the current neuroinflammation markers are targeting the TSPO in mitochondria, its uptake during imaging can originate from multiple sources. Separation of monocyte, astrocyte and microglial signal, by specific markers for the different cells involved is high priority for future ligand development. New targets for neuroinflammation imaging other than TSPO are a necessity in the future. The research related to the P2X7 receptor might provide a new and interesting path for the development of novel radioligands, in which the M2CAO model validated in study IV could prove to be beneficial.

Future of knock-out animals in PET

At present the most widely used animal species for producing gene knockout animals is the mouse. Its advantage over other rodent species is obvious with faster reproduction and smaller required space, but in PET imaging their small brain size and consequently smaller brain structures provide a disadvantage as an animal model for neuroscience. A normal mouse has a cortical thickness of 1.2 mm while larger sized rodents like rats show a cortical thickness of 1.8 mm *(24)*. While the mouse cortex is possibly still effected by partial volume effect even with the currently achieved advancements of under mm resolutions, larger rodent brains like rat or guinea pig is more likely to be devoid of measurement errors originating from small brain regions. Thus development of small animal knockouts other than mouse is advantageous for the future of functional *in vivo* PET imaging.

7 ACKNOWLEDGEMENTS

I would like to express my sincere gratitude and appreciation to all the brilliant minds that I've had the chance to meet and work with during the past years. This thesis would have not been possible without your contribution. I'm especially grateful to:

Professor Balázs Gulyás, my main supervisor, for guiding my way during the past years and for believing in me from the first day. Thank you for sharing your enthusiasm and deep knowledge in PET neuroscience.

Professor Christer Halldin, my co-supervisor, for his invaluable support and the always spot on observations that helped forming critical thinking.

Associate Professor Andrea Varrone, my co-supervisor, for always being available and for showing that one must not look at difficulties as an obstacle but rather as a fun challenge.

Professor Lars Farde for his comments that make you look at things from a different angle.

Dr. Martin Schain, my comrade in arms, for being the person he is and for his friendship. Dr. Anton Forsberg for the long conversations on science, life or even on the success of different polygon projections. Dr. Jenny Häggkvist for her clear mind in science, inspiration and for the long hours spent in the lab. Granville Matheson and Pontus Plaven Sigray for being beacons in the dark. Dr. Magdalena Nord, Dr. Patrik Fazio, Dr. Shigeyuki Yamamoto and Dr. Marie Svedberg for the fun discussions.

Sara Lundqvist and Björn Wolbert for providing professional and entertaining support during the PET experiments. Dr. Kálmán Nagy for sharing insights in physics and engineering.

Karin Zahir for always being helpful no matter how dire the situation was.

Dr. Akihiro Takano, Dr. Sjoerd Finnema, Dr. Per Stenkrona, Dr. Katarina Varnäs, Dr. Zsolt Cselényi and Dr. Simon Cervenka for their knowledge and helpfulness when I turned to them with scientific questions.

Dr. Janine Doorduin, Dr. Philip Little and Professor Staffan Holmin for the great collaboration and scientific debates.

All current and previous colleagues at Karolinska Institutet's PET imaging group: Dr. Pavitra Kannan, Susanna Nevala, Zsolt Sarnyai, Adam Lada, Gudrun Nylén, Siv Erikksson, Urban Hannsson, Carsten Steiger, Dr. Jan Andersson, Dr. Magnus Scou, Dr. Peter Johnström, Julio Gabriel and all the members of radiochemistry for their excellent assistance: Dr. Sangram Nag, Dr. Vladimir Stepanov, Guennadi Jogolev, Nahid Amini, Mahabuba Jahan, Dr. Zhisheng Jia, Arsalan Amir, Kenneth Dahl, Dr. Ryuji Nakao, Hanna Jacobson Ingemyr, Obaidur Rahman, Nándor Kaposy, Steffan Martinsson and Henrik Alfredéen, who also has some fine books to borrow.

Professor Károly Gulya for pushing me into the wilderness, where without his encouragement I wouldn’t have dared to go.

Finally, but not last, I’m grateful to my family for their continuous support (*Anya, Apa és Milán köszönöm, hogy hittetek bennem és hogy támogattatok.*), and I thank especially Lenke for her love and care, I couldn’t have gone through this journey without you.

8 REFERENCES

1. M. Bergström, A. Grahnén, B. Långström, Positron emission tomography microdosing: a new concept with application in tracer and early clinical drug development., *European journal of clinical pharmacology* **59**, 357–66 (2003).
2. C. Halldin, B. Gulyás, L. Farde, PET studies with carbon-11 radioligands in neuropsychopharmacological drug development., *Curr. Pharm. Des.* **7**, 1907–29 (2001).
3. C Halldin, B Gulyás, O Langer, Brain radioligands--state of the art and new trends., *The quarterly journal of nuclear medicine* (2001).
4. M. Honer, L. Gobbi, L. Martarello, R. Comley, Radioligand development for molecular imaging of the central nervous system with positron emission tomography, *Drug Discovery Today* **19**, 19361944 (2014).
5. M. Piel, I. Vernaleken, F. Rösch, Positron emission tomography in CNS drug discovery and drug monitoring., *Journal of Medicinal Chemistry* **57**, 92329258 (2014).
6. P. Colombino, B. Fiscella, L. Trossi, Study of positronium in water and ice from 22 to-144 C by annihilation quanta measurements, *Il Nuovo Cimento Series 10* **38**, 707–723 (1965).
7. S. Tong, A. Alessio, P. Kinahan, Image reconstruction for PET/CT scanners: past achievements and future challenges, *Imaging in Medicine* **2**, 529545 (2010).
8. L. Shepp, Y. Vardi, Maximum likelihood reconstruction for emission tomography., *IEEE transactions on medical imaging* **1**, 113–22 (1982).
9. R. Innis, V. Cunningham, J. Delforge, M. Fujita, A. Gjedde, R. Gunn, J. Holden, S. Houle, S.-C. Huang, M. Ichise, H. Iida, H. Ito, Y. Kimura, R. Koeppe, G. Knudsen, J. Knuuti, A. Lammertsma, M. Laruelle, J. Logan, R. Maguire, M. Mintun, E. Morris, R. Parsey, J. Price, M. Slifstein, V. Sossi, T. Suhara, J. Votaw, D. Wong, R. Carson, Consensus nomenclature for in vivo imaging of reversibly binding radioligands., *Journal of cerebral blood flow and metabolism* **27**, 1533–9 (2007).
10. J. Logan, J. Fowler, N. Volkow, A. Wolf, S. Dewey, D. Schlyer, R. MacGregor, R. Hitzemann, B. Bendriem, S. Gatley, D. Christman, Graphical Analysis of Reversible Radioligand Binding from Time-Activity Measurements Applied to [N-11C-methyl]-(-)-Cocaine PET Studies in Human Subjects, *Journal of Cerebral Blood Flow & Metabolism* **10**, 740–7 (1990).
11. R. Carson, Tracer kinetic modeling in PET, *Positron Emission Tomography:Basic Science and Clinical Practice*, Springer London, 127–159 (2005).
12. A. Lammertsma, C. Bench, S. Hume, S. Osman, K. Gunn, D. Brooks, R. Frackowiak, Comparison of Methods for Analysis of Clinical [11C]Raclopride Studies, *Journal of Cerebral Blood Flow & Metabolism* **16**, 42–52 (1996).
13. A. Lammertsma, S. Hume, Simplified Reference Tissue Model for PET Receptor Studies, *NeuroImage* **4**, 153158 (1996).
14. B. Pichler, M. Judenhofer, C. Pfannenberg, Multimodal Imaging Approaches: PET/CT and PET/MRI, *Handbook of Experimental Pharmacology: Molecular Imaging I, Springer Berlin Heidelberg*, 109–132 (2008).
15. P. Kinahan, D. Townsend, T. Beyer, D. Sashin, Attenuation correction for a combined 3D PET/CT scanner, *Medical Physics* **25**, 2046 (1998).
16. R. Weissleder, Scaling down imaging: molecular mapping of cancer in mice, *Nature Reviews Cancer* **2**, 11–18 (2002).
17. G. Brix, U. Lechel, G. Glatting, S. Ziegler, W. Münzing, S. Müller, T. Beyer, Radiation exposure of patients undergoing whole-body dual-modality 18F-FDG PET/CT examinations., *Journal of nuclear medicine* **46**, 608–13 (2005).

18. H. Zaidi, M.-L. Montandon, D. Slosman, Magnetic resonance imaging-guided attenuation and scatter corrections in three-dimensional brain positron emission tomography., *Med Phys* **30**, 937–48 (2003).
19. H. Herzog, U. Pietrzyk, N. Shah, K. Ziemons, The current state, challenges and perspectives of MR-PET., *NeuroImage* **49**, 2072–82 (2010).
20. D. Bailey, H. Barthel, T. Beyer, R. Boellaard, B. Gückel, D. Hellwig, H. Herzog, B. Pichler, H. Quick, O. Sabri, K. Scheffler, H. Schlemmer, N. Schwenzer, H. Wehrl, Summary Report of the First International Workshop on PET/MR Imaging, March 19–23, 2012, Tübingen, Germany, *Molecular Imaging and Biology* **15**, 361–371 (2013).
21. K. Wienhard, M. Dahlbom, L. Eriksson, C. Michel, T. Bruckbauer, U. Pietrzyk, W.-D. Heiss, The ECAT EXACT HR: Performance of a New High Resolution Positron Scanner., *Journal of Computer Assisted Tomography* **18**, 110 (1994).
22. D. Oprea-Lager, M. Yaqub, I. Pieters, R. Reinhard, R. Moorselaar, A. Eertwegh, O. Hoekstra, A. Lammertsma, R. Boellaard, A Clinical and Experimental Comparison of Time of Flight PET/MRI and PET/CT Systems, *Molecular Imaging and Biology* (2015).
23. A. Varrone, N. Sjöholm, L. Eriksson, B. Gulyás, C. Halldin, L. Farde, Advancement in PET quantification using 3D-OP-OSEM point spread function reconstruction with the HRRT, *European Journal of Nuclear Medicine and Molecular Imaging* **36**, 1639–1650 (2009).
24. J. DeFelipe, The Evolution of the Brain, the Human Nature of Cortical Circuits, and Intellectual Creativity, *Frontiers in Neuroanatomy* **5** (2011).
25. P. Herscovitch, M. Raichle, M. Kilbourn, M. Welch, Positron Emission Tomographic Measurement of Cerebral Blood Flow and Permeability-Surface Area Product of Water Using [15O]Water and [11C]Butanol, *Journal of Cerebral Blood Flow & Metabolism* **7**, 527–542 (1987).
26. B. Gulyás, C. Halldin, New PET radiopharmaceuticals beyond FDG for brain tumor imaging., *The quarterly journal of nuclear medicine and molecular imaging* **56**, 173–90 (2012).
27. H.-W. Shen, X.-L. Jiang, F. Gonzalez, A.-M. Yu, Humanized transgenic mouse models for drug metabolism and pharmacokinetic research., *Current drug metabolism* **12**, 997–1006 (2011).
28. M. Katoh, N. Suzuyama, T. Takeuchi, S. Yoshitomi, S. Asahi, T. Yokoi, Kinetic analyses for species differences in P-glycoprotein-mediated drug transport., *Journal of pharmaceutical sciences* **95**, 2673–83 (2006).
29. N. Suzuyama, M. Katoh, T. Takeuchi, S. Yoshitomi, T. Higuchi, S. Asashi, T. Yokoi, Species differences of inhibitory effects on P-glycoprotein-mediated drug transport., *Journal of pharmaceutical sciences* **96**, 1609–18 (2007).
30. S. Syvänen, O. Lindhe, M. Palner, B. Kornum, O. Rahman, B. Långström, G. Knudsen, M. Hammarlund-Udenaes, Species differences in blood-brain barrier transport of three positron emission tomography radioligands with emphasis on P-glycoprotein transport., *Drug metabolism and disposition* **37**, 635–43 (2008).
31. B. Torbett, A. Baird, B. Eliceiri, Understanding the rules of the road: proteomic approaches to interrogate the blood brain barrier, *Front Neurosci* **9**, 70 (2015).
32. M. Simard, G. Arcuino, T. Takano, Q. Liu, M. Nedergaard, Signaling at the gliovascular interface., *The Journal of neuroscience* **23**, 9254–62 (2003).
33. P. Kannan, C. John, S. Zoghbi, C. Halldin, M. Gottesman, R. Innis, M. Hall, Imaging the function of P-glycoprotein with radiotracers: pharmacokinetics and in vivo applications., *Clinical pharmacology and therapeutics* **86**, 368–77 (2009).
34. V. Braniste, M. Al-Asmakh, C. Kowal, F. Anuar, A. Abbaspour, M. Tóth, A. Korecka, N. Bakocevic, N. Guan, P. Kundu, B. Gulyás, C. Halldin, K. Hultenby,

H. Nilsson, H. Hebert, B. Volpe, B. Diamond, S. Pettersson, The gut microbiota influences blood-brain barrier permeability in mice., *Science translational medicine* **6**, 263ra158 (2014).
35. T. Azad, J. Pan, I. Connolly, A. Remington, C. Wilson, G. Grant, Therapeutic strategies to improve drug delivery across the blood-brain barrier., *Neurosurg Focus* **38**, E9 (2015).
36. G. Szakács, J. Paterson, J. Ludwig, C. Booth-Genthe, M. Gottesman, Targeting multidrug resistance in cancer, *Nat Rev Drug Discov* **5**, 219–34 (2006).
37. K. Moitra, M. Dean, Evolution of ABC transporters by gene duplication and their role in human disease., *Biological chemistry* **392**, 29–37 (2011).
38. D. Miller, Regulation of ABC transporters at the blood–brain barrier, *Clin. Pharmacol Ther* **97**, 395–403 (2015).
39. Y. Hoshi, Y. Uchida, M. Tachikawa, T. Inoue, S. Ohtsuki, T. Terasaki, Quantitative atlas of blood-brain barrier transporters, receptors, and tight junction proteins in rats and common marmoset., *Journal of pharmaceutical sciences* **102**, 3343–55 (2013).
40. R. Shawahna, Y. Uchida, X. Declèves, S. Ohtsuki, S. Yousif, S. Dauchy, A. Jacob, F. Chassoux, C. Daumas-Duport, P.-O. Couraud, T. Terasaki, J.-M. Scherrmann, Transcriptomic and quantitative proteomic analysis of transporters and drug metabolizing enzymes in freshly isolated human brain microvessels., *Molecular pharmaceutics* **8**, 1332–41 (2011).
41. G. Singhal, E. Jaehne, F. Corrigan, C. Toben, B. Baune, Inflammasomes in neuroinflammation and changes in brain function: a focused review, *Frontiers in Neuroscience* **8** (2014).
42. G. Raivich, M. Bohatschek, C. Kloss, A. Werner, L. Jones, G. Kreutzberg, Neuroglial activation repertoire in the injured brain: graded response, molecular mechanisms and cues to physiological function, *Brain Research Reviews* **30**, 77–105 (1999).
43. M Monif, G Burnstock, DA Williams, Microglia: proliferation and activation driven by the P2X7 receptor, *The International journal of biochemistry & cell biology* (2010).
44. M. McCann, J. O'Callaghan, P. Martin, T. Bertram, Differential activation of microglia and astrocytes following trimethyl tin-induced neurodegeneration, (1996).
45. H.-K. Jeong, K. Ji, K. Min, E.-H. Joe, Brain Inflammation and Microglia: Facts and Misconceptions, *Exp Neurobiol* (2013).
46. DC Chugani, NL Kedersha, Vault immunofluorescence in the brain: new insights regarding the origin of microglia, *The Journal of Neuroscience* (1991).
47. L. Lawson, V. Perry, P. Dri, S. Gordon, Heterogeneity in the distribution and morphology of microglia in the normal adult mouse brain, *Neuroscience* **39**, 151–170 (1990).
48. A. Cardona, E. Pioro, M. Sasse, V. Kostenko, S. Cardona, I. Dijkstra, D. Huang, G. Kidd, S. Dombrowski, R. Dutta, J.-C. Lee, D. Cook, S. Jung, S. Lira, D. Littman, R. Ransohoff, Control of microglial neurotoxicity by the fractalkine receptor, *Nat Neurosci* (2006).
49. K. Saijo, J. Collier, A. Li, J. Katzenellenbogen, C. Glass, An ADIOL-ERβ-CtBP Transrepression Pathway Negatively Regulates Microglia-Mediated Inflammation, *Cell* (2011).
50. M. Chen, T. Guilarte, Translocator protein 18 kDa (TSPO): molecular sensor of brain injury and repair, (2008), doi:10.1016/j.pharmthera.2007.12.004.
51. R. Soccio, J. Breslow, Intracellular Cholesterol Transport, *Arteriosclerosis, Thrombosis, and Vascular Biology* **24**, 1150–1160 (2004).

52. M. Gavish, I. Bachman, R. Shoukrun, Y. Katz, L. Veenman, G. Weisinger, A. Weizman, Enigma of the peripheral benzodiazepine receptor., *Pharmacological reviews* **51**, 629–50 (1999).
53. V. Papadopoulos, M. Baraldi, T. Guilarte, T. Knudsen, J.-J. Lacapère, P. Lindemann, M. Norenberg, D. Nutt, A. Weizman, M.-R. Zhang, M. Gavish, Translocator protein (18 kDa): new nomenclature for the peripheral-type benzodiazepine receptor based on its structure and molecular function, *Trends in Pharmacological Sciences* **27** (2006).
54. K.-R. Bae, H.-J. Shim, D. Balu, S. Kim, S.-W. Yu, Translocator protein 18 kDa negatively regulates inflammation in microglia., *Journal of neuroimmune pharmacology* **9**, 424–37 (2014).
55. K. Virdee, P. Cumming, D. Caprioli, B. Jupp, A. Rominger, F. Aigbirhio, T. Fryer, P. Riss, J. Dalley, Applications of positron emission tomography in animal models of neurological and neuropsychiatric disorders., *Neuroscience and biobehavioral reviews* **36**, 1188–216 (2012).
56. R. Banati, Visualising microglial activation in vivo, *Glia* **40**, 206–217 (2002).
57. H. Boutin, F. Chauveau, C. Thominiaux, B. Kuhnast, M. Grégoire, S. Jan, R. Trebossen, F. Dollé, B. Tavitian, F. Mattner, A. Katsifis, In vivo imaging of brain lesions with [11C]CLINME, a new PET radioligand of peripheral benzodiazepine receptors, *Glia* **55**, 1459–1468 (2007).
58. M. Imaizumi, H.-J. Kim, S. Zoghbi, E. Briard, J. Hong, J. Musachio, C. Ruetzler, D.-M. Chuang, V. Pike, R. Innis, M. Fujita, PET imaging with [11C]PBR28 can localize and quantify upregulated peripheral benzodiazepine receptors associated with cerebral ischemia in rat., *Neuroscience letters* **411**, 200–5 (2007).
59. M. Imaizumi, E. Briard, S. Zoghbi, J. Gourley, J. Hong, Y. Fujimura, V. Pike, R. Innis, M. Fujita, Brain and whole-body imaging in nonhuman primates of [11C]PBR28, a promising PET radioligand for peripheral benzodiazepine receptors., *NeuroImage* **39**, 1289–98 (2008).
60. A. Wilson, A. Garcia, J. Parkes, P. McCormick, K. Stephenson, S. Houle, N. Vasdev, Radiosynthesis and initial evaluation of [18F]-FEPPA for PET imaging of peripheral benzodiazepine receptors., *Nuclear medicine and biology* **35**, 305–14 (2008).
61. F. Chauveau, N. Camp, F. Dollé, B. Kuhnast, F. Hinnen, A. Damont, H. Boutin, M. James, M. Kassiou, B. Tavitian, Comparative evaluation of the translocator protein radioligands 11C-DPA-713, 18F-DPA-714, and 11C-PK11195 in a rat model of acute neuroinflammation., *Journal of nuclear medicine* **50**, 468–76 (2009).
62. Q. Guo, D. Owen, E. Rabiner, F. Turkheimer, R. Gunn, Identifying improved TSPO PET imaging probes through biomathematics: the impact of multiple TSPO binding sites in vivo., *NeuroImage* **60**, 902–10 (2012).
63. AK Brown, M Fujita, Y Fujimura, JS Liow, Radiation dosimetry and biodistribution in monkey and man of 11C-PBR28: a PET radioligand to image inflammation, *Journal of Nuclear Medicine* (2007).
64. W. Kreisl, M. Fujita, Y. Fujimura, N. Kimura, K. Jenko, P. Kannan, J. Hong, C. Morse, S. Zoghbi, R. Gladding, S. Jacobson, U. Oh, V. Pike, R. Innis, Comparison of [(11)C]-(R)-PK 11195 and [(11)C]PBR28, two radioligands for translocator protein (18 kDa) in human and monkey: Implications for positron emission tomographic imaging of this inflammation biomarker., *NeuroImage* **49**, 2924–32 (2010).
65. D. Owen, O. Howell, S.-P. Tang, L. Wells, I. Bennacef, M. Bergstrom, R. Gunn, E. Rabiner, M. Wilkins, R. Reynolds, P. Matthews, C. Parker, Two binding sites for [3H]PBR28 in human brain: implications for TSPO PET imaging of

neuroinflammation., *Journal of cerebral blood flow and metabolism* **30**, 1608–18 (2010).
66. D. Owen, A. Yeo, R. Gunn, K. Song, G. Wadsworth, A. Lewis, C. Rhodes, D. Pulford, I. Bennacef, C. Parker, P. StJean, L. Cardon, V. Mooser, P. Matthews, E. Rabiner, J. Rubio, An 18-kDa translocator protein (TSPO) polymorphism explains differences in binding affinity of the PET radioligand PBR28., *Journal of cerebral blood flow and metabolism* **32**, 1–5 (2012).
67. R. Myers, L. Manjil, B. Cullen, G. Price, R. Frackowiak, J. Cremer, Macrophage and astrocyte populations in relation to [3H]PK 11195 binding in rat cerebral cortex following a local ischaemic lesion., *Journal of cerebral blood flow and metabolism* **11**, 314–22 (1991).
68. D. Stephenson, D. Schober, E. Smalstig, R. Mincy, D. Gehlert, J. Clemens, Peripheral benzodiazepine receptors are colocalized with activated microglia following transient global forebrain ischemia in the rat., *The Journal of neuroscience* **15**, 5263–74 (1995).
69. S. Rojas, A. Martín, M. Arranz, D. Pareto, J. Purroy, E. Verdaguer, J. Llop, V. Gómez, J. Gispert, O. Millán, Á. Chamorro, A. Planas, Imaging brain inflammation with [11C]PK11195 by PET and induction of the peripheral-type benzodiazepine receptor after transient focal ischemia in rats, *Journal of Cerebral Blood Flow & Metabolism* **27**, 1975–1986 (2007).
70. S. Lavisse, M. Guillermier, A.-S. Hérard, F. Petit, M. Delahaye, N. Camp, L. Haim, V. Lebon, P. Remy, F. Dollé, T. Delzescaux, G. Bonvento, P. Hantraye, C. Escartin, Reactive Astrocytes Overexpress TSPO and Are Detected by TSPO Positron Emission Tomography Imaging, *The Journal of Neuroscience* **32**, 10809–10818 (2012).
71. J. Beavo, M. Houslay, S. Francis, in Cyclic Nucleotide Phosphodiesterases in Health and Disease. (CRC Press).
72. C Lugnier, Cyclic nucleotide phosphodiesterase (PDE) superfamily: a new target for the development of specific therapeutic agents, *Pharmacology & therapeutics* (2006).
73. E. Salter, A. Wierzbicki, The Mechanism of Cyclic Nucleotide Hydrolysis in the Phosphodiesterase Catalytic Site, *The Journal of Physical Chemistry B* **111**, 45474552 (2007).
74. S. Soderling, J. Beavo, Regulation of cAMP and cGMP signaling: new phosphodiesterases and new functions, *Current Opinion in Cell Biology* **12**, 174179 (2000).
75. M. Houslay, G. Milligan, Tailoring cAMP-signalling responses through isoform multiplicity, (1997).
76. T. Seeger, B. Bartlett, T. Coskran, J. Culp, L. James, D. Krull, J. Lanfear, A. Ryan, C. Schmidt, C. Strick, A. Varghese, R. Williams, P. Wylie, F. Menniti, Immunohistochemical localization of PDE10A in the rat brain., *Brain research* **985**, 113–26 (2003).
77. T. Coskran, D. Morton, F. Menniti, W. Adamowicz, R. Kleiman, A. Ryan, C. Strick, C. Schmidt, D. Stephenson, Immunohistochemical Localization of Phosphodiesterase 10A in Multiple Mammalian Species, *Journal of Histochemistry & Cytochemistry* **54**, 1205–13 (2006).
78. A. HEBB, H. ROBERTSON, Role of phosphodiesterases in neurological and psychiatric disease, *Current Opinion in Pharmacology* **7**, 8692 (2007).
79. J. Siuciak, D. Chapin, J. Harms, L. Lebel, S. McCarthy, L. Chambers, A. Shrikhande, S. Wong, F. Menniti, C. Schmidt, Inhibition of the striatum-enriched phosphodiesterase PDE10A: A novel approach to the treatment of psychosis, *Neuropharmacology* **51**, 386–396 (2006).

80. A. Harada, K. Suzuki, S. Miura, T. Hasui, N. Kamiguchi, T. Ishii, T. Taniguchi, T. Kuroita, A. Takano, V. Stepanov, C. Halldin, H. Kimura, Characterization of the binding properties of T-773 as a PET radioligand for phosphodiesterase 10A, *Nuclear Medicine and Biology* **42**, 146154 (2015).
81. L. Wilson, N. Brandon, Emerging biology of PDE10A., *Current pharmaceutical design* **21**, 378–88 (2015).
82. A. Hebb, H. Robertson, E. Denovan-Wright, Striatal phosphodiesterase mRNA and protein levels are reduced in Huntington's disease transgenic mice prior to the onset of motor symptoms., *Neuroscience* **123**, 967–81 (2004).
83. R. Kleiman, L. Kimmel, S. Bove, T. Lanz, J. Harms, A. Romegialli, K. Miller, A. Willis, S. Etages, M. Kuhn, C. Schmidt, Chronic suppression of phosphodiesterase 10A alters striatal expression of genes responsible for neurotransmitter synthesis, neurotransmission, and signaling pathways implicated in Huntington's disease., *The Journal of pharmacology and experimental therapeutics* **336**, 64–76 (2011).
84. J. Siuciak, The role of phosphodiesterases in schizophrenia : therapeutic implications., *CNS Drugs* **22**, 983–93 (2008).
85. Z. Tu, J. Xu, L. Jones, S. Li, R. Mach, Carbon-11 labeled papaverine as a PET tracer for imaging PDE10A: radiosynthesis, in vitro and in vivo evaluation, (2010).
86. S. Celen, M. Koole, M. Angelis, I. Sannen, S. Chitneni, J. Alcazar, S. Dedeurwaerdere, D. Moechars, M. Schmidt, A. Verbruggen, X. Langlois, K. Laere, J. Andrés, G. Bormans, Preclinical evaluation of 18F-JNJ41510417 as a radioligand for PET imaging of phosphodiesterase-10A in the brain., *Journal of nuclear medicine* **51**, 1584–91 (2010).
87. C Plisson, C Salinas, D Weinzimmer, D Labaree, Radiosynthesis and in vivo evaluation of [11 C] MP-10 as a positron emission tomography radioligand for phosphodiesterase 10A, *Nuclear medicine and Biology* (2011).
88. O Barret, D Thomae, D Alagille, H Lee, First in vivo assessment of two PDE10 tracers [18F] MNI654 and [18F] MNI659, *Journal of Nuclear Medicine* (2012).
89. O. Barret, D. Thomae, A. Tavares, D. Alagille, In vivo assessment and dosimetry of 2 novel PDE10A PET radiotracers in humans: 18F-MNI-659 and 18F-MNI-654, *Journal of Nuclear Medicine* (2014).
90. V. K. Laere, RU Ahmad, H Hudyana, S Celen, Human biodistribution and dosimetry of 18F-JNJ42259152, a radioligand for phosphodiesterase 10A imaging, *European Journal of Nuclear Medicine and Molecular Imaging* (2013).
91. DR Hwang, E Hu, S Rumfelt, B Easwaramoorthy, Initial characterization of a PDE10A selective positron emission tomography tracer [11 C] AMG 7980 in non-human primates, *Nuclear Medicine and Biology* (2014).
92. M. Kelly, N. Brandon, Differential function of phosphodiesterase families in the brain: gaining insights through the use of genetically modified animals., *Prog. Brain Res.* **179**, 67–73 (2009).
93. J. Siuciak, S. McCarthy, D. Chapin, A. Martin, J. Harms, C. Schmidt, Behavioral characterization of mice deficient in the phosphodiesterase-10A (PDE10A) enzyme on a C57/Bl6N congenic background., *Neuropharmacology* (2008).
94. H. Sano, Y. Nagai, T. Miyakawa, R. Shigemoto, M. Yokoi, Increased social interaction in mice deficient of the striatal medium spiny neuron-specific phosphodiesterase 10A2., *J. Neurochem.* **105**, 546–56 (2008).
95. M. Pierson, J. Andersson, S. Nyberg, D. McCarthy, S. Finnema, K. Varnäs, A. Takano, P. Karlsson, B. Gulyás, A. Medd, C.-M. Lee, M. Powell, J. Heys, W. Potts, N. Seneca, L. Mrzljak, L. Farde, C. Halldin, [11C]AZ10419369: a selective 5-HT1B receptor radioligand suitable for positron emission tomography (PET). Characterization in the primate brain., *NeuroImage* **41**, 1075–85 (2008).

96. J. Andersson, M. Pierson, S. Finnema, B. Gulyás, R. Heys, C. Elmore, L. Farde, C. Halldin, Development of a PET radioligand for the central 5-HT1B receptor: radiosynthesis and characterization in cynomolgus monkeys of eight radiolabeled compounds., *Nuclear medicine and biology* **38**, 261–72 (2011).
97. E. Briard, S. Zoghbi, M. Imaizumi, J. Gourley, H. Shetty, J. Hong, V. Cropley, M. Fujita, R. Innis, V. Pike, Synthesis and evaluation in monkey of two sensitive 11C-labeled aryloxyanilide ligands for imaging brain peripheral benzodiazepine receptors in vivo., *Journal of medicinal chemistry* **51**, 17–30 (2008).
98. V. Stepanov, S. Miura, A. Takano, H. Kimura, T. Taniguchi, C. Halldin, Development of a Series of Novel Carbon-11 Labeled PDE10A Inhibitors., *Journal of Labelled Compounds and Radiopharmaceuticals* **56**, S492 (2013).
99. C. Halldin, L. Farde, T. Högberg, N. Mohell, H. Hall, T. Suhara, P. Karlsson, Y. Nakashima, C.-G. Swahn, Carbon-11-FLB 457: a radioligand for extrastriatal D2 dopamine receptors., *Journal of nuclear medicine* **36**, 1275–1281 (1995).
100. A. Laupacis, Cyclosporin A: a powerful immunosuppressant, *Canadian Medical Association Journal* **126** (1982).
101. D. Tedesco, L. Haragsim, Cyclosporine: A Review, *Journal of Transplantation* **2012** (2012).
102. A. Sakata, I. Tamai, K. Kawazu, Y. Deguchi, T. Ohnishi, A. Saheki, A. Tsuji, In vivo evidence for ATP-dependent and P-glycoprotein-mediated transport of cyclosporin A at the blood-brain barrier., *Biochemical pharmacology* **48**, 1989–92 (1994).
103. L. Jetté, G. Murphy, J. Leclerc, R. Beliveau, Interaction of drugs with P-glycoprotein in brain capillaries., *Biochemical pharmacology* **50**, 1701–9 (1995).
104. N. Hendrikse, E. Vries, L. Eriks-Fluks, W. Graaf, G. Hospers, A. Willemsen, W. Vaalburg, E. Franssen, A new in vivo method to study P-glycoprotein transport in tumors and the blood-brain barrier., *Cancer research* **59**, 2411–6 (1999).
105. A. El-Sheikh, R. Greupink, H. Wortelboer, J. Heuvel, M. Schreurs, J. Koenderink, R. Masereeuw, F. Russel, Interaction of immunosuppressive drugs with human organic anion transporter (OAT) 1 and OAT3, and multidrug resistance-associated protein (MRP) 2 and MRP4., *Translational research* **162**, 398–409 (2013).
106. L. Li, Q. Yao, S. Xu, H. Hu, Q. Shen, Y. Tian, L. Pan, H. Zhou, H. Jiang, C. Lu, L. Yu, S. Zeng, Cyclosporin A affects the bioavailability of ginkgolic acids via inhibition of P-gp and BCRP, *European Journal of Pharmaceutics and Biopharmaceutics* **88**, 759767 (2014).
107. K. Letschert, H. Faulstich, D. Keller, D. Keppler, Molecular characterization and inhibition of amanitin uptake into human hepatocytes., *Toxicological sciences* **91**, 140–9 (2006).
108. A. Treiber, R. Schneiter, S. Häusler, B. Stieger, Bosentan is a substrate of human OATP1B1 and OATP1B3: inhibition of hepatic uptake as the common mechanism of its interactions with cyclosporin A, rifampicin, and sildenafil., *Drug metabolism and disposition* **35**, 1400–7 (2007).
109. H. W. de Jong, F. H. van Velden, R. W. Kloet, F. L. Buijs, R. Boellaard, A. A. Lammertsma, Performance evaluation of the ECAT HRRT: an LSO-LYSO double layer high resolution, high sensitivity scanner., *Phys Med Biol* **52**, 1505–26 (2007).
110. I. Szanda, J. Mackewn, G. Patay, P. Major, K. Sunassee, G. Mullen, G. Nemeth, Y. Haemisch, P. Blower, P. Marsden, National Electrical Manufacturers Association NU-4 performance evaluation of the PET component of the NanoPET/CT preclinical PET/CT scanner., *J. Nucl. Med.* **52**, 1741–1747 (2011).
111. F. Arnberg, J. Lundberg, M. Söderman, P. Damberg, S. Holmin, Image-guided method in the rat for inducing cortical or striatal infarction and for controlling cerebral blood flow under MRI., *Stroke* **43**, 2437–43 (2012).

112. J. Mulder, E. Björling, K. Jonasson, H. Wernérus, S. Hober, T. Hökfelt, M. Uhlén, Tissue profiling of the mammalian central nervous system using human antibody-based proteomics., *Mol. Cell Proteomics* **8**, 1612–22 (2009).
113. R. Mullen, C. Buck, A. Smith, NeuN, a neuronal specific nuclear protein in vertebrates., *Development* **116**, 201–11 (1992).
114. D. Oksenberg, S. A. Marsters, B. F. O'Dowd, H. Jin, S. Havlik, S. J. Peroutka, A. Ashkenazi, A single amino-acid difference confers major pharmacological variation between human and rodent 5-HT1B receptors., *Nature* **360**, 161–3 (1992).
115. M. Schain, S. Benjaminsson, K. Varnäs, A. Forsberg, C. Halldin, A. Lansner, L. Farde, A. Varrone, Arterial input function derived from pairwise correlations between PET-image voxels, *Journal of Cerebral Blood Flow & Metabolism* **33**, 1058–1065 (2013).